International Journal of Mechanical Sciences 299 (2025) 110355

Contents lists available at ScienceDirect

International Journal of Mechanical Sciences

journal homepage: www.elsevier.com/locate/ijmecsci

Programmable inverse design framework for morphing hard-magnetic soft materials

Maoyuan Li [a,1], Yifan Yang [a,1], Ya Wen [a], Jizhai Cui [b], Wei Cheng [c], Enming Song [d], Fan Xu [a,*]

[a] Institute of Mechanics and Computational Engineering, Department of Aeronautics and Astronautics & College of Intelligent Robotics and Advanced Manufacturing, Fudan University, 220 Handan Road, Shanghai 200433, PR China
[b] International Institute for Intelligent Nanorobots and Nanosystems & College of Intelligent Robotics and Advanced Manufacturing, Fudan University, 220 Handan Road, Shanghai 200433, PR China
[c] Institute of Science and Technology for Brain-Inspired Intelligence, Fudan University, 220 Handan Road, Shanghai 200433, PR China
[d] Institute of Optoelectronics, Shanghai Frontiers Science Research Base of Intelligent Optoelectronics and Perception, Fudan University, Shanghai 200433, PR China

ARTICLE INFO

Keywords:
Inverse design
Magnetic actuators
Hard-magnetic beam
Optimization algorithm
Large deformation
Shape morphing

ABSTRACT

As a type of shape-programmable soft materials, hard-magnetic soft materials (HMSMs) exhibit rapid and reversible deformations under applied magnetic fields, showing promise for soft robotics, flexible electronics, and biomedical devices. The realization of various controllable shape transformations is crucial to the rational design of relevant applications. However, due to highly nonlinear relation between large deformations and actuation fields, how to quantitatively design the residual magnetization distribution and driving magnetic field in the initial configuration to morph into a target shape remains a challenge. Here, we propose an inverse design strategy for targeted bending dominated deformations of hard-magnetic beam structures, which combines a 3D hard-magnetic rod model with intelligent optimization algorithms, enabling hard-magnetic beams to achieve multi-step pre-designed shapes by programming the magnetization densities and external magnetic fields in the initial undeformed configuration. Based on the proposed framework, we explore diverse target shapes under various magnetization modes, and compare the numerical accuracy and efficiency of three intelligent optimization algorithms. Moreover, we demonstrate multi-step inverse design examples in which the same sample achieves a flexible transition of various pre-designed deformation modes. The results demonstrate that the presented strategy offers an innovative and versatile approach for programmable inverse design of morphing magnetically-driven flexible devices and soft robotics.

1. Introduction

Shape-programmable soft materials have the ability to sense external stimuli (e.g., light, temperature, humidity, electric field, magnetic field, etc.) and make deformation responses. They can transform between complex shapes and typically have one or several characteristics of rapid, reversible and reconfigurable deformation, remote controllability and shape memory. A series of shape-programmable soft materials include liquid crystal elastomers (LCEs) [1–3], hydrogels [4,5], magnetic soft materials [6,7], and shape memory polymers (SMPs) [8,9]. As one of them, hard-magnetic soft materials (HMSMs) can rapidly respond to the external magnetic field and have flexible programmability, which hold enormous potential for applications like flexible electronics [6,10,11], drug delivery [12,13], metamaterials [14–17], actuators [18], and soft robotics [7,19,20]. HMSMs are typically synthesized by incorporating hard-magnetic particles or discrete hard magnets into a soft matrix [21,22]. When subjected to an actuated magnetic field, these magnetization-saturated hard-magnetic particles produce internal torques. Therefore, the morphological transition of HMSMs is achieved through pre-designed magnetization distributions and directions [23–25]. In general, the programming magnetization distribution of HMSMs is based on nonuniform hard-magnetic particle distribution (magnetization density magnitude) [20,26] or anisotropic hard-magnetic domains (magnetization density direction) [6,7,27]. The properties regarding residual magnetization are generally established during the device fabrication stage, combining advanced manufacturing techniques and novel design concepts [6,27–30], resulting in significant progress in biomimetic soft robots and functional devices. [28] reported a novel manufacturing technique with two components: a passive component

* Corresponding author.
E-mail address: fanxu@fudan.edu.cn (F. Xu).
[1] These authors contributed equally to this work.

https://doi.org/10.1016/j.ijmecsci.2025.110355
Received 24 January 2025; Received in revised form 1 May 2025; Accepted 5 May 2025
Available online 22 May 2025

and an active component, which can create a beam with varying magnitude and direction of magnetization density. [7] obtained a multimodal motion soft robot with axially varying magnetization directions by wrapping a hard-magnetic beam around a cylinder for magnetization. [6] reported a 3D printing technique combined with a magnetic field that can quickly print HMSM structures with programmed ferromagnetic domains, enabling rapid morphing from 2D shapes to complex 3D configurations. Inspired by their work, [31] proposed a "voxel-encoding DIW printing" method that enables HMSMs to have different magnetization density magnitudes through the combination of multiple layers. [32] used 3D printing and packaging techniques to produce hard-magnetic beams with anisotropic magnetization profiles for biomimetic applications. [20] developed a hard-magnetic beam with nonuniform distribution of magnetic particles to build magnetic soft continuum robots (MSCRs). Additionally, [29] developed a method based on ultraviolet (UV) lithography that can achieve 3D magnetization profile programming for HMSMs. The laser-rewritable magnetic composite film reported by [30] and the magnetic dynamic polymer (MDP) composite developed by [27] can achieve reprogramming of the magnetization profile. [33] proposed a magnetization programming method based on the structural buckling instability phenomenon, providing a template-free and on-demand manner for the formation of HMSMs with 3D continuous nonuniform magnetization profiles. [34] developed a high-remanence hard-magnetic photosensitive suspension for 3D printing shape-programmable soft actuators.

To harness the programmable deformation potential and enable rational structure design of HMSMs, significant efforts have been made on quantitative prediction of the deformation behavior of HMSMs. [35] developed a theoretical framework of the ideal HMSMs constitutive model and established a finite element simulation framework, verified by [6,27,31]. Based on the work of [35,36] considered viscoelastic effects of HMSMs. [37] derived nonlinear formulas for finite deformation analysis of HMSMs based on the micropolar continuum theory [38] and explored the viscoelastic effect [39]. [40] derived a meshfree model based on the radial point interpolation method to describe nonlinear behaviors of HMSMs, enabling rational designs of programmable locomotion modes in flexible robotics. [41] developed a finite-strain solid-shell model to predict shape morphing of magneto-elastic structures without plane stress or Kirchhoff assumptions, which demonstrates superior computational efficiency and accuracy than the traditional eight-node brick element [35]. In addition, there exist some studies on the theoretical modeling of HMSMs from the micromechanics standpoint [42–44]. When considering geometric characteristic of most slender structures, the modeling of HMSMs can be simply viewed as beam- and rod-like structures. [45] proposed a large deformation beam model of HMSMs [35], focusing on the deformation of a slender hard-magnetic beam with a uniform magnetization along the body under uniform magnetic fields, which has been applied in the design of ferromagnetic soft continuum robots [19]. [26] focused on the mechanical responses of a functionally graded hard-magnetic soft (FGHMS) beam with a continuously varying volume fraction of hard-magnetic particles actuated by a uniform external magnetic field. [46] proposed an extensible variable curvature hard-magnetic soft beam model based on the Timoshenko shear deformation theory. [47] provided a comprehensive framework based on reduced-order theory to predict the response of hard-magnetic beams under magnetic excitation, focusing on nonuniform magnetic fields with constant gradients. Following the Kirchhoff hypotheses, [48] established a reduced-order framework to analyze hard-magnetic rods, investigating the deformation of straight and curved rods with magnetization densities perpendicular to the axial direction under either constant or constant-gradient magnetic fields. [49] applied the co-rotational method to decouple rigid-body motions from spatial deformations of slender hard-magnetic elastica, which dramatically enhanced computational performance compared with traditional solid element [35].

Prior works have mainly focused on modeling the "forward problem", which involves predicting the deformation of *a prior* given HMSMs structure under external magnetic actuation. However, achieving programmable deformations into arbitrary target shapes remains a crucial challenge in shape-morphing systems [50], namely inverse design. Various approaches have emerged across different actuation mechanisms. [51] demonstrated an approach to achieve programmed shape-morphing by encoding the distribution and direction of modular-designed hinges. [52] explored the inverse design of programmable shape-morphing kirigami structures, while [53] developed a design framework for 3D-printed thermally activated shape-morphing structures. [54] proposed a modeling approach for programmable morphing structures with variable stiffness, and [55] studied curved-creased origami metamaterials with programmable stability and stiffness. Additionally, [56] demonstrated the shape programming of porous bilayer hydrogel structures, and [57] applied topology optimization for arbitrary curvature programming of thermo-active liquid crystal elastomers. For HMSMs, the key lies in providing a solution for the initial magnetization distribution and driving magnetic field based on target deformed shapes, namely inverse design. Due to highly nonlinear relation between large deformations and actuation fields of HMSMs, there are only few works on inverse design. [28] developed a programming methodology to represent the magnetization density and actuating magnetic field in terms of a 1D Fourier series. They generated the required magnetization profile and actuating magnetic fields for HMSMs by optimizing the coefficients of Fourier series to obtain time-varying shapes. [32] proposed a shape-programming strategy to derive the magnetic moments and actuating magnetic fields required to transform HMSMs into stable shapes. [31] employed an evolutionary algorithm (EA) to design the magnetization distribution and applied DIW printing technology to fabricate magnetic voxels for assembling structures, thereby achieving the desired curvatures. [20] optimized the workspace of magnetic soft continuum robots (MSCRs) by integrating a theoretical model and the genetic algorithm (GA). These optimization strategies mainly focus on beam-like structures. [58] developed a multi-physics topology optimization framework for the inverse design of magneto-active kirigami metasurfaces, bio-inspired robotic motion and actuation. [59] presented a framework for optimizing hard-magnetic soft materials for programmable deformations, which was later applied to the design of magneto-mechanical metamaterials [60]. [61] introduced a multiphysics topology optimization framework that concurrently optimizes topologies and continuous remanent magnetization distributions in the magnetic soft materials and structures. However, most current design strategies are based on a single target shape, which can only handle relatively simple scenarios.

Here, we propose an inverse design strategy for targeted deformations of hard-magnetic slender structures, which enables hard-magnetic beam networks to achieve pre-designed shapes by programming magnetization densities and external magnetic fields. We establish a functional relation between the deformed shape of the beam and its magnetization density and external magnetic field using a 3D hard-magnetic rod model, thus transforming the inverse problem of bending deformation into a highly nonlinear and non-derivable function extremum problem that can be solved by intelligent optimization algorithms. We demonstrate the optimization results of hard-magnetic beam structures under three magnetization density programming modes through several representative examples, and weigh up the pros and cons of three intelligent optimization algorithms, which evaluates the performance of the inverse design strategy of programmable morphing. Moreover, we design complex optimization cases involving multi-step deformations of the hard-magnetic beam networks and cellular thin-walled structures. Our framework provides an effective and versatile tool for inversely designing programmable shape-morphing structures driven by magnetic fields.

The paper is organized as follows. In Section 2, a 3D hard-magnetic rod model is presented including the theoretical framework and computational method. In Section 3, a programmable inverse design strategy

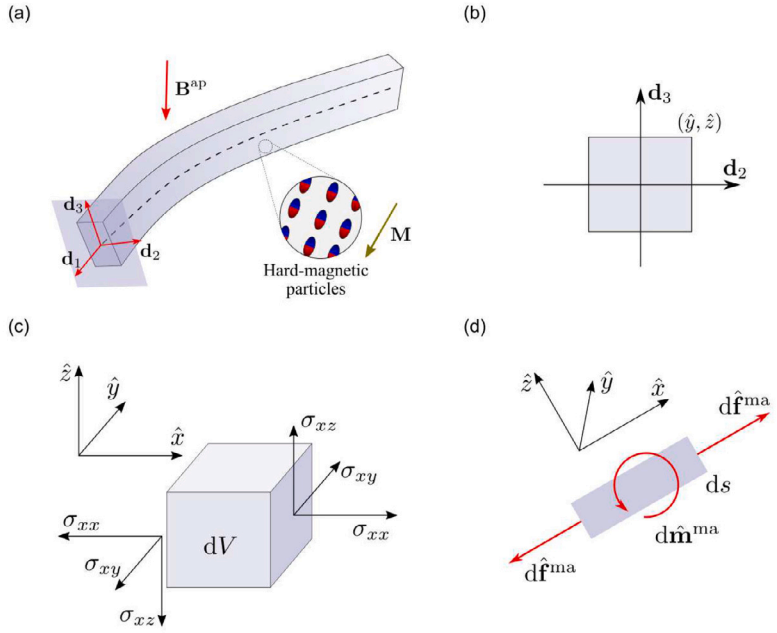

Fig. 1. Coordinates of a flexible hard-magnetic rod and its force equilibrium. (a) A rod with permanent magnetization $\mathbf{M}$ subject to applied magnetic fields $\mathbf{B}^{\mathrm{ap}}$. (b) Cross-sectional local coordinate system $(\hat{y}, \hat{z})$. Schematic of force states: (c) infinitesimal volume element and (d) 1D line element.

of morphing hard-magnetic materials is established. The inverse design problem is firstly transformed into the minimum value problem of the error function, and then solved by three intelligent optimization algorithms (genetic algorithm, particle swarm optimization, and simulated annealing algorithm). To demonstrate the flexibility and effectiveness of the proposed inverse design framework, we explore numerous examples with diverse structures in Section 4.

2. A 3D hard-magnetic rod model

In this section, we construct a forward model for the inverse design of hard-magnetic structures. We apply a 3D hard-magnetic rod model [49] to compute large deformations of hard-magnetic slender structures. Compared with other finite element models, this model only needs a small number of elements to ensure numerical accuracy, and the superior computational efficiency is particularly important in the subsequent iterative optimization process in the inverse design.

As shown in Fig. 1(a), we investigate a rod of length L, width W, and thickness H, exhibiting isotropic elasticity described by mechanical properties such as Poisson's ratio ν, shear modulus G and Young's modulus $E = 2(1+\nu)G$. Note that geometric nonlinearity of the slender structure plays more important role than material nonlinearity under applied magnetic stimuli [41]. In large-deflection bending deformations driven by small-magnitude magnetic fields, the axial elongation remains relatively small (typically less than 0.01 [62]), and thus predictions of linear elasticity are consistent with hyperelastic laws [41]. Therefore, linear elastic law appears to be sufficient to accurately describe the bending dominated deformation behavior. Here, the extensible Kirchhoff hypothesis is adopted, assuming that the rod allows large displacement and rotation but small strain, without shear deformation. For the slender HMSMs beams considered here, the Kirchhoff rod theory provides an adequate description of bending deformations, and shear effects are negligible for beams with high aspect ratio [46]. The flexible rod is simplified as a 1D structure, characterized by a centerline $\mathbf{r}(s)$ with arc-length parameter $s \in [0, L]$ [63,64]. Three unit basis vectors $\{\mathbf{d}_1 = \mathbf{r}'(s), \mathbf{d}_2, \mathbf{d}_3\}$ define the cross-section orientation (see Fig. 1(a)). The curvature vector $\boldsymbol{\kappa} = \kappa_1\mathbf{d}_1 + \kappa_2\mathbf{d}_2 + \kappa_3\mathbf{d}_3$ comprises torsional curvature κ_1 about $\mathbf{d}_1$, and bending curvatures κ_2 and κ_3 about $\mathbf{d}_2$ and $\mathbf{d}_3$, respectively. Using coordinates $(\hat{x}, \hat{y}, \hat{z})$ with respect to the basis $\{\mathbf{d}_1, \mathbf{d}_2, \mathbf{d}_3\}$, for any point $(\hat{y}, \hat{z})$ in the cross-sectional plane $(\mathbf{d}_2, \mathbf{d}_3)$ (see Fig. 1(b)), strains are given by

$$\begin{cases} \varepsilon_{11} = \varepsilon_m - \hat{y}\kappa_3 + \hat{z}\kappa_2, \\ \varepsilon_{12} = -\hat{z}\kappa_1, \\ \varepsilon_{13} = \hat{y}\kappa_1, \end{cases} \tag{1}$$

where ε_m is the axial strain along $\mathbf{d}_1$. Then, the stress tensor is obtained by

$$\begin{bmatrix} \sigma_{11} \\ \sigma_{12} \\ \sigma_{13} \end{bmatrix} = \begin{bmatrix} E & 0 & 0 \\ 0 & G & 0 \\ 0 & 0 & G \end{bmatrix} \begin{bmatrix} \varepsilon_{11} \\ \varepsilon_{12} \\ \varepsilon_{13} \end{bmatrix}, \tag{2}$$

in which $\sigma_{22} = \sigma_{23} = \sigma_{32} = \sigma_{33} = 0$. The strain energy of the rod can be written as

$$\begin{aligned} W^{\mathrm{el}} &= \int_V \frac{1}{2}\left(\sigma_{11}\varepsilon_{11} + \sigma_{12}\varepsilon_{12} + \sigma_{13}\varepsilon_{13}\right) \mathrm{d}V \\ &= \int_0^L \frac{1}{2}\left(EA\varepsilon_m^2 + GI_1\kappa_1^2 + EI_2\kappa_2^2 + EI_3\kappa_3^2\right) \mathrm{d}s, \end{aligned} \tag{3}$$

in which A denotes the cross-sectional area and the corresponding moments of inertia are given by

$$I_2 = \int_A \hat{z}^2 \mathrm{d}A, \quad I_3 = \int_A \hat{y}^2 \mathrm{d}A, \quad I_1 = I_2 + I_3. \tag{4}$$

The variational form of Eq. (3) reads

$$\delta W^{\mathrm{el}} = \int_0^L (\mathbf{f}^{\mathrm{el}} \cdot \mathbf{d}_1 \delta\varepsilon_m + \mathbf{m}^{\mathrm{el}} \cdot \mathbf{d}_1 \delta\kappa_1 + \mathbf{m}^{\mathrm{el}} \cdot \mathbf{d}_2 \delta\kappa_2 + \mathbf{m}^{\mathrm{el}} \cdot \mathbf{d}_3 \delta\kappa_3) \mathrm{d}s, \tag{5}$$

where the direction of the elastic force $\mathbf{f}^{\mathrm{el}}$ aligns with the vector $\mathbf{d}_1$ and $\mathbf{m}^{\mathrm{el}}$ denotes the torque, given by

$$\begin{cases} \mathbf{f}^{\mathrm{el}} = EA\varepsilon_m \mathbf{d}_1, \\ \mathbf{m}^{\mathrm{el}} = GI_1\kappa_1\mathbf{d}_1 + EI_2\kappa_2\mathbf{d}_2 + EI_3\kappa_3\mathbf{d}_3. \end{cases} \tag{6}$$

We employ an ideal constitutive framework for hard-magnetic elastomers [35,65] to characterize the effects of applied magnetic fields. Recent work indicates that the remanent magnetization in HMSMs depends on rotation rather than stretching, as magnetic particles are

too rigid to stretch compared to the polymeric matrix. Considering the **R**-based magnetic potential [66], $\phi^{\mathrm{ma}} = -\mathbf{RM}\cdot\mathbf{B}^{\mathrm{ap}}$, the magnetic first Piola–Kirchhoff stress can be expressed as [67]

$$\mathbf{P}^{\mathrm{ma}} = -\left(\frac{\partial \mathbf{R}}{\partial \mathbf{F}}\right)^{T}\left[\mathbf{B}^{\mathrm{ap}}\otimes\mathbf{M}\right], \tag{7}$$

where **F** is the deformation gradient and **R** is the rigid-body rotation. Under deformations involving large rotations and small stretches, we neglect the effect of stretching in magnetic potential energy with $\mathbf{F}\sim\mathbf{R}$, and the Cauchy stress can be represented as

$$\boldsymbol{\sigma}^{\mathrm{ma}} = -\frac{1}{J}\mathbf{B}^{\mathrm{ap}}\otimes\mathbf{RM} = -\mathbf{B}^{\mathrm{ap}}\otimes\mathbf{M}^{\mathrm{cur}}, \tag{8}$$

in which **M** and $\mathbf{M}^{\mathrm{cur}}$ represent the internal remanent magnetization of materials in the initial and current configuration, respectively. The applied magnetic field is denoted by $\mathbf{B}^{\mathrm{ap}}$ and $\otimes$ indicate the tensor product operation. Note that the presence of body couples due to magnetic-mechanical coupling inherently leads to an asymmetric Cauchy stress tensor [37,68], which has provided satisfactory predictions for slender HMSM structures [35,47]. This theoretical framework requires spatially uniform external magnetic fields and homogeneously distributed magnetic particles [69]. Additionally, the magnetic flux density induced in the material is assumed to be linearly related to the external field strength at small magnitudes. When the external magnetic field is non-uniform, e.g., if the sample is too close to the magnetic actuation source, interactions between the boundary and the magnetic field must be considered. Similarly, the geometric boundaries of the samples have considerable effects. The non-uniformity of magnetic fields near the bulk specimen corners may be non-negligible, while it is less pronounced in slender structures. In such cases, the magnetic flux needs to be regarded as an unknown field that requires full-field analysis combining boundary conditions and the displacement field [70].

The incompressibility condition of the material requires $J = \det(\mathbf{F}) = 1$. For an infinitesimal volume element in the local coordinate system $\mathbf{d}_1, \mathbf{d}_2, \mathbf{d}_3$ (Fig. 1(c)), the magnetic stress $\boldsymbol{\sigma}^{\mathrm{ma}}$ reads

$$\sigma_{ij}^{\mathrm{ma}} = -\hat{B}_i^{\mathrm{ap}}\hat{M}_j^{\mathrm{cur}}. \tag{9}$$

For planes orthogonal to $\mathbf{d}_1$, expressions for magnetic force and moment are written as

$$\begin{cases} \mathrm{d}\hat{\mathbf{f}}_{11}^{\mathrm{ma}} = \sigma_{11}^{\mathrm{ma}}\mathrm{d}\hat{y}\mathrm{d}\hat{z}\mathbf{d}_1, \\ \mathrm{d}\hat{\mathbf{m}}_{13}^{\mathrm{ma}} = -\sigma_{13}^{\mathrm{ma}}\mathrm{d}\hat{y}\mathrm{d}\hat{z}\cdot\mathrm{d}\hat{x} = -\sigma_{13}^{\mathrm{ma}}\mathrm{d}V\mathbf{d}_2, \\ \mathrm{d}\hat{\mathbf{m}}_{12}^{\mathrm{ma}} = \sigma_{12}^{\mathrm{ma}}\mathrm{d}V\mathbf{d}_3. \end{cases} \tag{10}$$

Similar expressions can be derived for the $\mathbf{d}_2$ and $\mathbf{d}_3$ orientations. Consequently, the total magnetic force and moment within the volumetric element (see Fig. 1(d)) can be represented by

$$\mathrm{d}\hat{\mathbf{f}}^{\mathrm{ma}} = \sigma_{11}^{\mathrm{ma}}\mathrm{d}\hat{y}\mathrm{d}\hat{z}\mathbf{d}_1 + \sigma_{22}^{\mathrm{ma}}\mathrm{d}\hat{z}\mathrm{d}\hat{x}\mathbf{d}_2 + \sigma_{33}^{\mathrm{ma}}\mathrm{d}\hat{x}\mathrm{d}\hat{y}\mathbf{d}_3, \tag{11}$$

$$\begin{aligned} \mathrm{d}\hat{\mathbf{m}}^{\mathrm{ma}} &= (-\sigma_{13}^{\mathrm{ma}}\mathbf{d}_2 + \sigma_{32}^{\mathrm{ma}}\mathbf{d}_2 + \sigma_{12}^{\mathrm{ma}}\mathbf{d}_3 - \sigma_{21}^{\mathrm{ma}}\mathbf{d}_3 - \sigma_{32}^{\mathrm{ma}}\mathbf{d}_1 + \sigma_{23}^{\mathrm{ma}}\mathbf{d}_1)\mathrm{d}V \\ &= \hat{\mathbf{M}}^{\mathrm{cur}}\times\hat{\mathbf{B}}^{\mathrm{ap}}\mathrm{d}V. \end{aligned} \tag{12}$$

Within the Kirchhoff rod theory, the analysis focuses on $\mathbf{d}_1$ direction, yielding $\mathrm{d}\hat{\mathbf{f}}^{\mathrm{ma}} = \sigma_{11}^{\mathrm{ma}}\mathrm{d}\hat{y}\mathrm{d}\hat{z}\mathbf{d}_1$. By integrating $\mathrm{d}\hat{\mathbf{f}}^{\mathrm{ma}}$ and $\mathrm{d}\hat{\mathbf{m}}^{\mathrm{ma}}$ across the cross-sectional area, one obtains

$$\begin{aligned} &\hat{\mathbf{f}}^{\mathrm{ma}} = -\hat{\mathrm{B}}_1^{\mathrm{ap}}\hat{\mathrm{M}}_1^{\mathrm{cur}}A\mathbf{d}_1, \\ &\frac{\mathrm{d}\hat{\mathbf{m}}^{\mathrm{ma}}}{\mathrm{d}s} = \mathbf{M}^{\mathrm{cur}}\times\mathbf{B}^{\mathrm{ap}}A. \end{aligned} \tag{13}$$

The interaction between external magnetic fields and magnetization is equivalent to a longitudinal force $\hat{\mathbf{f}}^{\mathrm{ma}}$ in the direction $\mathbf{d}_1$ and a torque $\hat{\mathbf{m}}^{\mathrm{ma}}$. For numerical implementation, we discretize the 3D magnetically-actuated beam using rod elements with two nodes. A co-rotational approach is adopted to remove rigid-body motion [71]. We solve the system through explicit time integration within an updated Lagrangian (UL) framework [72]. The complete numerical scheme is presented in Appendix A.

3. Inverse design strategy for hard-magnetic beams

In this section, we develop an inverse design framework combining intelligent optimization algorithms. For a hard-magnetic beam, the distribution of its magnetization density **M** (magnitude and direction) determines its deformation under the applied magnetic field $\mathbf{B}^{\mathrm{ap}}$. To morph the hard-magnetic beam into a target shape, *i.e.,* programming its magnetization density **M**, applied magnetic field $\mathbf{B}^{\mathrm{ap}}$ and other parameters, we convert the inverse problem into a numerical optimization problem for solving the minimum value by intelligent optimization algorithms. The process of solving the inverse problem is illustrated in Fig. 2(a).

In computations, each magnetic beam is divided into N elements with a total of $N+1$ nodes by two-node rod element. The target bending shape of the magnetic beam is represented by the coordinates at corresponding $N+1$ nodes, denoted by $\mathbf{x}_{\mathrm{ex}}^i$ $(i = 1, 2, \ldots, N+1)$. Therefore, one needs to solve the magnetic density distribution of the hard-magnetic beam on each element $\mathbf{M}^j$ $(j = 1, 2, \ldots, N)$ to minimize the deviation between the actual and target shapes. Here, we take the parameter set $\{\mathbf{M}^j, \mathbf{B}^{\mathrm{ap}}\}$ to be designed as an independent variable. For any set of parameters $\{\mathbf{M}^j, \mathbf{B}^{\mathrm{ap}}\}$, the bending deformation shape of hard-magnetic beams can be calculated through the hard-magnetic rod model, that is, the corresponding node coordinate $\{\mathbf{x}_{\mathrm{n}}^i\}$ $(i = 1, 2, \ldots, N+1)$. Then the difference between the node coordinates $\{\mathbf{x}_{\mathrm{n}}^i\}$ $(i = 1, 2, \ldots, N+1)$ calculated and the node coordinates $\{\mathbf{x}_{\mathrm{ex}}^i\}$ $(i = 1, 2, \ldots, N+1)$ on the target function is used to describe the shape error, and the relative error function is defined as

$$f\left(\{\mathbf{M}^j, \mathbf{B}^{\mathrm{ap}}\}\right) = \frac{\sum_{i=1}^{N+1} |\{\mathbf{x}_{\mathrm{ex}}^i\} - \{\mathbf{x}_{\mathrm{n}}^i\}|}{\sum_{i=1}^{N+1} |\{\mathbf{x}_{\mathrm{ex}}^i\}|}. \tag{14}$$

In this way, the inverse design problem of parametric magnetization density **M** and applied magnetic field $\mathbf{B}^{\mathrm{ap}}$ can be transformed into a minimum value problem of the relative error function (14). Since this kind of mapping extremum problem is highly nonlinear and non-derivable, we adopt three different intelligent optimization algorithms (genetic algorithm, particle swarm optimization, and simulated annealing algorithm) to solve it (see Fig. 2(b)). These nature-inspired algorithms demonstrate adaptive problem-solving capabilities by simulating natural processes and collective intelligence. Specifically, genetic algorithms mimic evolutionary principles through selection, crossover, and mutation operators. Particle swarm optimization simulates the social dynamics of bird flocking or fish schooling where individuals share information to guide the swarm, and simulated annealing replicates the controlled cooling process in metallurgy to reach optimal states. These approaches enable the algorithms to learn from iterations, adapt their search strategies, and make probabilistic decisions when exploring the solution space. Another key advantage of these methods is that they do not require gradient information, making them particularly suitable for the non-differentiable and discontinuous problem. Compared to gradient-descent based algorithms [73–76], these algorithms can better handle multimodal optimization problems and avoid getting trapped in local optima. Moreover, unlike data-driven approaches [77], they do not require large amounts of pre-collected training data. Detailed description of algorithms can be found in Appendix B.

4. Results and discussion

We explore a series of cases that present the capabilities and effectiveness of the proposed inverse design strategy of hard-magnetic beam structures. Section 4.1 explores target shapes under three different magnetization modes, compares the numerical efficiency of three intelligent optimization algorithms, and evaluates the effectiveness of the programmable inverse design strategy. Section 4.2 demonstrates multi-step inverse design examples in which the samples achieve a flexible transition between different pre-designed shapes. Section 4.3 presents an optimization case for spatial deformations of complex hard-magnetic network structures. The proposed inverse design framework of hard-magnetic beam structures is implemented using in-house Matlab code.

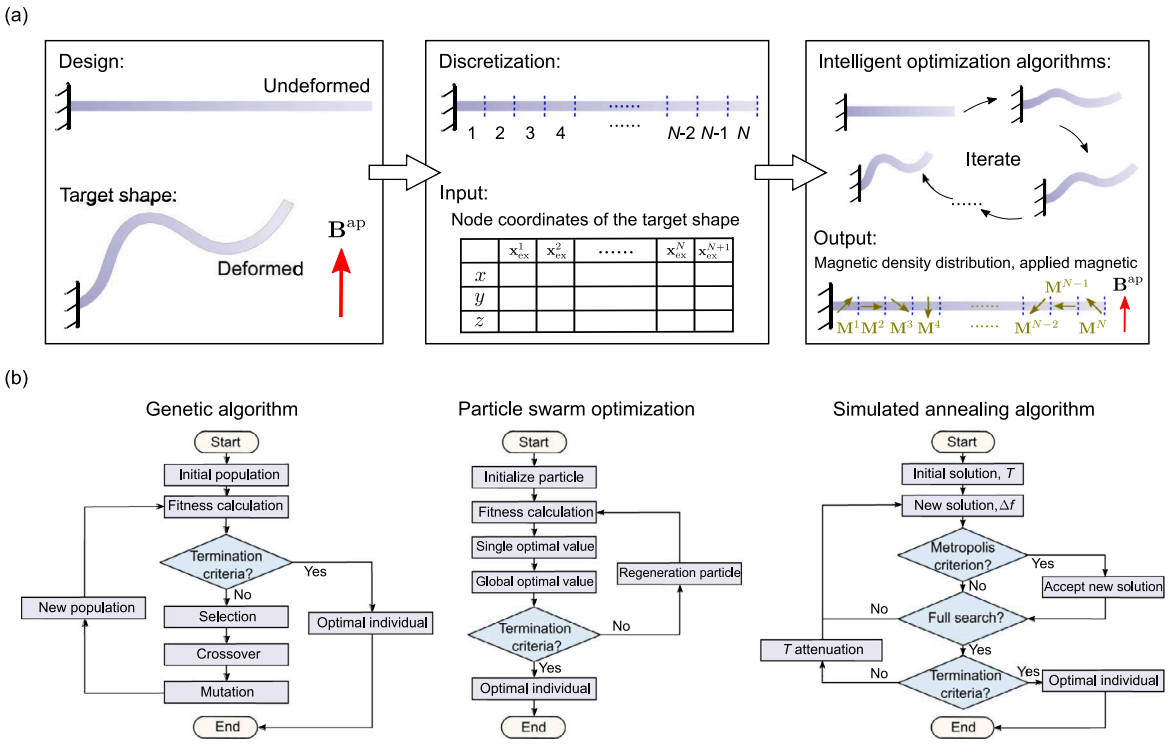

Fig. 2. Overview of the inverse design framework for hard-magnetic beam deformations. (a) Flow chart for solving the inverse problem of hard-magnetic beam deformation. (b) Flow charts of three intelligent optimization algorithms.

Table 1
A hard-magnetic beam deforms into the target shape $z = 0.03x^2$ under the excitation of applied magnetic field $\mathbf{B}^{ap} = 10\mathbf{d}_3$ mT. Distributions of magnetic density $\mathbf{M}$ are calculated iteratively by three intelligent optimization algorithms in the continuous domain of magnetization intensity $|\mathbf{M}| = 0 \sim 114$ kA/m.

Algorithm	Element	1(2)	3(4)	5(6)	7(8)	9(10)	11(12)	13(14)	15(16)	17(18)	19(20)	Error (%)
GA	$\|\mathbf{M}\|$ (A/m)	777	1601	4900	30 846	8725	8151	5042	19 352	11 848	23 703	0.66
PSO	$\|\mathbf{M}\|$ (A/m)	49 696	0	0	0	9259	0	30 940	4140	33 088	21 362	0.17
SA	$\|\mathbf{M}\|$ (A/m)	1101	1989	938	4426	8006	844	33 482	43 509	14 468	594	0.40

4.1. Inverse design of hard-magnetic beams with large deformation

Let us first demonstrate the feasibility of the inverse design strategy by achieving the bending deformation of several simple shapes of hard-magnetic beams. Here, a cantilever beam with a length of $L = 17.5$ mm and a square cross-section ($W = H = 0.875$ mm) is analyzed. The beam is discretized into $n = 20$ elements. The simulation parameters include a total duration of $t = 2$ s, time increment of $\Delta t = 1\times10^{-5}$ s, and damping coefficient $\zeta = 20$. The external magnetic field is gradually increased with a linear ramp-up from zero to maximum value during the first step of simulation ($0 \sim 0.5t$), followed by a constant value for the rest ($0.5t \sim t$) to reach equilibrium. In the inverse design, the magnetization density $\mathbf{M}$ of the hard-magnetic beam is divided into ten segments.

4.1.1. Inverse problem solving on continuous domain

In this section, we assume that the magnetization density $\mathbf{M}$ is along the axis of the hard-magnetic beam (positive direction of the x-axis) and the magnitude can vary continuously in the range of $0 \sim 114$ kA/m. The hard-magnetic beam will transform into the target shape $z = 0.03x^2$ under the excitation of applied magnetic field $\mathbf{B}^{ap} = 10\mathbf{d}_3$ mT. The relation between magnetization intensity $|\mathbf{M}|$, shear modulus G of hard-magnetic soft materials and volume fraction of magnetic particles ϕ satisfies [19]

$$|\mathbf{M}| = M_p\phi,$$
$$G = G_0\exp\left(\frac{2.5\phi}{1-3.5\phi}\right), \tag{15}$$

where M_p and G_0 denote the magnetization of magnetic particles and the shear modulus of pure matrix without particles, respectively. The volume fraction of magnetic particles is typically limited to $\sim 30\%$. Therefore, the design of magnetization density $\mathbf{M}$ of the hard-magnetic beam turns out to be the design of the volume density of the magnetic particles, and thus the shear modulus G of the hard-magnetic beam is no longer constant. [62] calculated such functionally graded hard-magnetic soft beams with varying volume fractions of magnetic particles. The material parameters $M_p = 513$ kA/m and $G_0 = 137$ kPa are adopted here [35]. Note that we have simplified our model by neglecting the interactions of internal magnetic fields between different regions. These interactions may become significant when the volume fraction of magnetic particles is large [78].

As shown in Fig. 3, genetic algorithm (GA), particle swarm optimization algorithm (PSO) and simulated annealing algorithm (SA) are respectively employed for optimization. The population number and algebra of the GA are set as 100 and 50, respectively. To maintain the consistency of the overall number of iterations of different algorithms, the total numbers of particles and iterations of the PSO are respectively set as 100 and 50 as well. The number of the SA is set as 5000 since it has only one individual in the optimization process. The optimization processes of three algorithms are illustrated in Fig. 3(a)–(c). The blue dots and black dots represent the (average) results and the optimal solutions of the current generation, respectively. The resulting distributions of the magnetization density $\mathbf{M}$ and their errors are shown in Table 1. It can be seen that the three algorithms obtain different results but all with error less than 1%, indicating the multi-solution of the nonlinear problem. The design diagram of the hard-magnetic beam corresponding

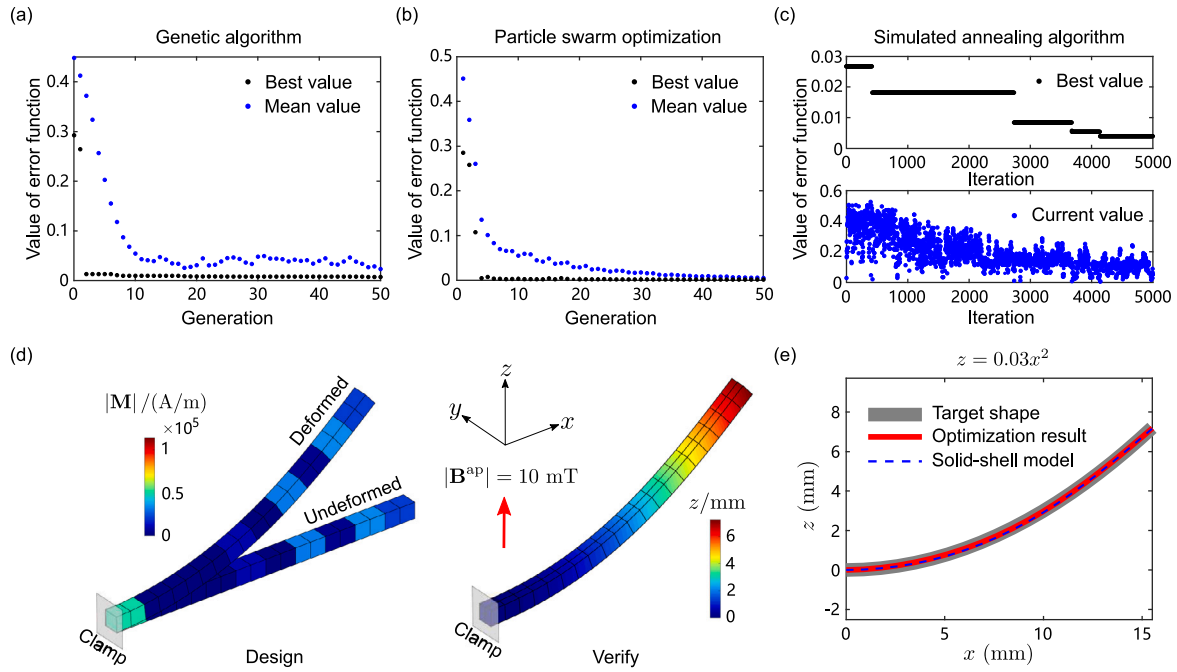

Fig. 3. A hard-magnetic beam deforms into the target shape $z = 0.03x^2$ under the excitation of applied magnetic field $\mathbf{B}^{ap} = 10\mathbf{d}_3$ mT. Three intelligent optimization algorithms are used to solve the inverse problem in the continuous domain of magnetization intensity $|\mathbf{M}| = 0 \sim 114$ kA/m. (a) Optimization process of genetic algorithm (GA). (b) Optimization process of particle swarm optimization algorithm (PSO). (c) Optimization process of simulated annealing algorithm (SA). The blue and black dots represent (average) results and optimal solutions of the current generation, respectively. (d) Design of the hard-magnetic beam with minimum error (0.17%) in the optimization results. (e) Comparison of the target shape, optimization result and solid-shell model [41].

Table 2
A hard-magnetic beam deforms into the target shape $z = 3[1 - \cos(0.06\pi x)]$ under the excitation of applied magnetic field $\mathbf{B}^{ap} = 20\mathbf{d}_3$ mT. Distributions of magnetic density $\mathbf{M}$ are calculated iteratively by three intelligent optimization algorithms in the discrete domain with magnetization intensity $|\mathbf{M}|$ ={-114, −76, −38, 0, 38, 76, 114} kA/m.

Algorithm	Element	1(2)	3(4)	5(6)	7(8)	9(10)	11(12)	13(14)	15(16)	17(18)	19(20)	Error (%)
GA	$\|\mathbf{M}\|$ (kA/m)	0	0	114	−38	38	76	114	76	−76	−114	0.75
PSO	$\|\mathbf{M}\|$ (kA/m)	38	38	76	0	114	−76	114	76	−114	−38	0.34
SA	$\|\mathbf{M}\|$ (kA/m)	76	−38	76	76	0	38	114	0	−76	−38	0.71

Table 3
A hard-magnetic beam deforms into the target shape $x = \sqrt{R^2 - (z - R)^2}$, where $R = L/\pi$ under the excitation of applied magnetic field $\mathbf{B}^{ap} = 30\mathbf{d}_1$ mT. Distributions of magnetic density $\mathbf{M}$ are calculated iteratively by three intelligent optimization algorithms in the mixed domain with magnetization intensity $|\mathbf{M}|$ ={0, 38, 76, 114} kA/m and its direction $\theta^{\mathbf{M}} = 0° \sim 360°$.

Algorithm	Element	1(2)	3(4)	5(6)	7(8)	9(10)	11(12)	13(14)	15(16)	17(18)	19(20)	Error (%)
GA	$\|\mathbf{M}\|$ (kA/m)	38	76	0	76	38	76	76	114	114	114	1.80
	$\theta^{\mathbf{M}}$ (°)	198.3	158.8	0	16.6	224.5	240.5	194.3	226.3	168.3	161.8	
PSO	$\|\mathbf{M}\|$ (kA/m)	114	76	114	76	114	114	76	114	114	114	0.40
	$\theta^{\mathbf{M}}$ (°)	148.5	225.5	0.5	224.0	331.9	215.4	282.0	225.3	135.0	100.0	
SA	$\|\mathbf{M}\|$ (kA/m)	38	76	76	114	114	38	114	114	76	114	1.78
	$\theta^{\mathbf{M}}$ (°)	174.7	98.5	127.2	224.1	208.3	175.3	164.7	164.3	59.9	101.0	

to the result with the minimum error (0.17%) is drawn in Fig. 3(d). The optimized deformation profile of the hard-magnetic beam in Fig. 3(e) shows a good agreement with the target shape, which indicates the effectiveness of the optimization strategy. Note that increasing the number of population (particles) and iterations of the optimization can reduce the error, but the algorithms would tend to be cumbersome and the computational cost dramatically increases.

4.1.2. *Inverse problem solving on discrete domain*

We next assume that the magnetization density $\mathbf{M}$ is along the axis of the hard-magnetic beam but its magnitude can only vary within a given set {-114, -76, -38, 0, 38, 76, 114} kA/m. The hard-magnetic beam transforms into the target shape $z = 3[1 - \cos(0.06\pi x)]$ under the excitation of applied magnetic field $\mathbf{B}^{ap} = 20\mathbf{d}_3$ mT. [31] developed a voxel-encoding printing technique to make such hard-magnetic soft materials. Each section of the hard-magnetic beam is divided into three layers and the magnetization density $\mathbf{M}$ of each layer can be {-38, 0, 38} kA/m. Note that 0 kA/m here refers to the "inactive layer" without the magnetizing process, but it contains magnetic particles with the same volume fraction as the other layers. This processing method discretizes the value range of magnetic density $\mathbf{M}$, which is more conducive to the production and application of hard-magnetic beams [31]. Therefore, unlike the previous section, the shear modulus of the whole hard-magnetic beam remains constant ($G = 303$ kPa). The magnetization density $\mathbf{M}$ of the whole segment is the vector summation of three layers, so there are seven cases of magnetization density $\mathbf{M}$ of each segment ($\{-114, -76, -38, 0, 38, 76, 114\}$ kA/m), and totally 7^{10} cases of magnetization density $\mathbf{M}$ distribution in the whole hard-magnetic beam.

The optimization processes of three algorithms are respectively described in Fig. 4(a)–(c), where the blue dots and black dots represent

Table 4
The tentacles of two hard-magnetic swimming robots deform into the target parabolic shapes ($z_1 = 0.05x_1^2$, $z_2 = -0.2x_2^2$) or sine waves ($z_1 = 3\left[1-\cos\left(0.06\pi x_1\right)\right]$, $z_2 = -6\left[1-\cos\left(0.07\pi x_2\right)\right]$) under the excitation of two-step applied magnetic field $\mathbf{B}_1^{\mathrm{ap}}$ and $\mathbf{B}_2^{\mathrm{ap}}$. Distributions of magnetic density $\mathbf{M}$ and two-step applied magnetic field are calculated iteratively by three intelligent optimization algorithms in the mixed domain with magnetization intensity $|\mathbf{M}|$ ={0, 38, 76, 114} kA/m, its direction $\theta^{\mathbf{M}} = 0° \sim 360°$, and applied magnetic fields $|\mathbf{B}_1^{\mathrm{ap}}| = 0 \sim 30$ mT and $|\mathbf{B}_2^{\mathrm{ap}}| = -30 \sim 0$ mT.

Shape	Algorithm	Element	1(2)	3(4)	5(6)	7(8)	9(10)	11(12)	13(14)	15(16)	17(18)	19(20)	$\lvert\mathbf{B}_1^{\mathrm{ap}}\rvert$(mT)	$\lvert\mathbf{B}_2^{\mathrm{ap}}\rvert$(mT)	Error(%)
Para-bola	GA	$\lvert\mathbf{M}\rvert$ (kA/m)	114	0	114	114	38	0	76	76	38	114	15.8	−29.5	4.14
		$\theta^{\mathbf{M}}$ (°)	312.1	217.0	27.3	72.2	33.6	0	248.4	27.5	276.3	17.2			
	PSO	$\lvert\mathbf{M}\rvert$ (kA/m)	114	114	114	114	0	0	0	0	0	114	23.4	−25.8	3.52
		$\theta^{\mathbf{M}}$ (°)	0	0	105.3	39.7	0	0	0	0	0	359.5			
	SA	$\lvert\mathbf{M}\rvert$ (kA/m)	76	114	76	114	114	114	114	0	0	114	15.9	−28.3	4.25
		$\theta^{\mathbf{M}}$ (°)	264.2	53.8	98.8	0.9	14.4	40.9	175.2	0	0	309.5			
Sine	GA	$\lvert\mathbf{M}\rvert$ (kA/m)	76	0	114	114	114	76	0	38	76	76	20.8	−24.3	2.85
		$\theta^{\mathbf{M}}$ (°)	55.4	0	63.5	32.2	36.2	310.4	0	34.4	242.2	146.7			
	PSO	$\lvert\mathbf{M}\rvert$ (kA/m)	114	114	0	0	38	114	114	0	0	76	23.4	−29.9	3.69
		$\theta^{\mathbf{M}}$ (°)	15.3	14.8	0	0	12.4	353.7	104.6	0	0	236.0			
	SA	$\lvert\mathbf{M}\rvert$ (kA/m)	38	38	114	114	114	38	76	0	76	38	14.1	−21.9	3.69
		$\theta^{\mathbf{M}}$ (°)	63.0	257.5	355.5	29.9	37.2	321.7	144.6	0	299.3	141.8			

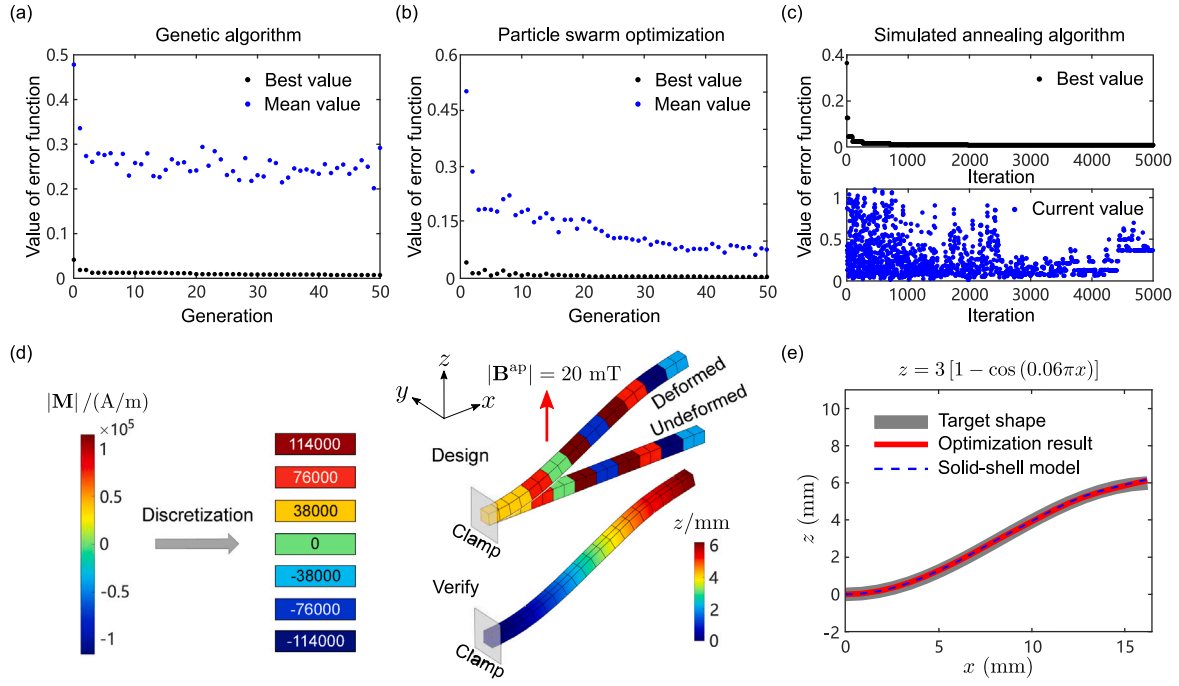

Fig. 4. A hard-magnetic beam deforms into the target shape $z = 3\left[1-\cos\left(0.06\pi x\right)\right]$ under the excitation of applied magnetic field $\mathbf{B}^{\mathrm{ap}} = 20\mathbf{d}_3$ mT. Three intelligent optimization algorithms are used to solve the inverse problem in the discrete domain with the magnetization intensity $|\mathbf{M}|$ = {-114, -76, -38, 0, 38, 76, 114} kA/m. (a) Optimization process of genetic algorithm (GA). (b) Optimization process of particle swarm optimization algorithm (PSO). (c) Optimization process of simulated annealing algorithm (SA). The blue and black dots represent (average) results and optimal solutions of the current generation, respectively. (d) Design of the hard-magnetic beam with minimum error (0.34%) in the optimization results. (e) Comparison of the target shape, optimization result and solid-shell model [41].

the (average) results and the optimal solution of the current generation, respectively. The resulting distributions of magnetization density $\mathbf{M}$ and their errors are shown in Table 2, where the errors of all three algorithms are less than 1%. The design diagrams of the hard-magnetic beam corresponding to the result with the minimum error (0.34%) are drawn in Figs. 4(d) and (e).

4.1.3. Hybrid inverse problem

We now consider a more general case with the direction of magnetization density $\mathbf{M}$ in the (x, z) plane, since Eq. (13) suggests that the direction of magnetic density $\mathbf{M}$ plays a key role in the deformation of the hard-magnetic beam. The angle $\theta^{\mathbf{M}}$ between the direction of magnetization density $\mathbf{M}$ and x-axis vary in the continuous domain $0° \sim 360°$, while the magnetization intensity $|\mathbf{M}|$ is chosen within the set {0, 38, 76, 114} kA/m. Therefore, the decomposition of magnetization density $\mathbf{M}$ in the reference configuration reads

$$\mathbf{M} = \left[|\mathbf{M}|\cos\theta^{\mathbf{M}} \quad 0 \quad |\mathbf{M}|\sin\theta^{\mathbf{M}}\right]^{\mathrm{T}}. \tag{16}$$

The hard-magnetic beam transforms into the target shape $x = \sqrt{R^2-(z-R)^2}$, where $R = L/\pi$ under the excitation of applied magnetic field $\mathbf{B}^{\mathrm{ap}} = 30\mathbf{d}_1$ mT. The optimization processes of three algorithms are respectively depicted in Figs. 5(a)–(c), in which the blue dots and black dots represent the (average) results and the optimal solution of the current generation, respectively. The resulting distributions of magnetization density $\mathbf{M}$ and their errors are shown in Table 3. The error of the result obtained by PSO algorithm remains the smallest (0.40%). The design diagram of the hard-magnetic beam corresponding to the result with the minimum error (0.40%) is drawn in Fig. 5(d). It

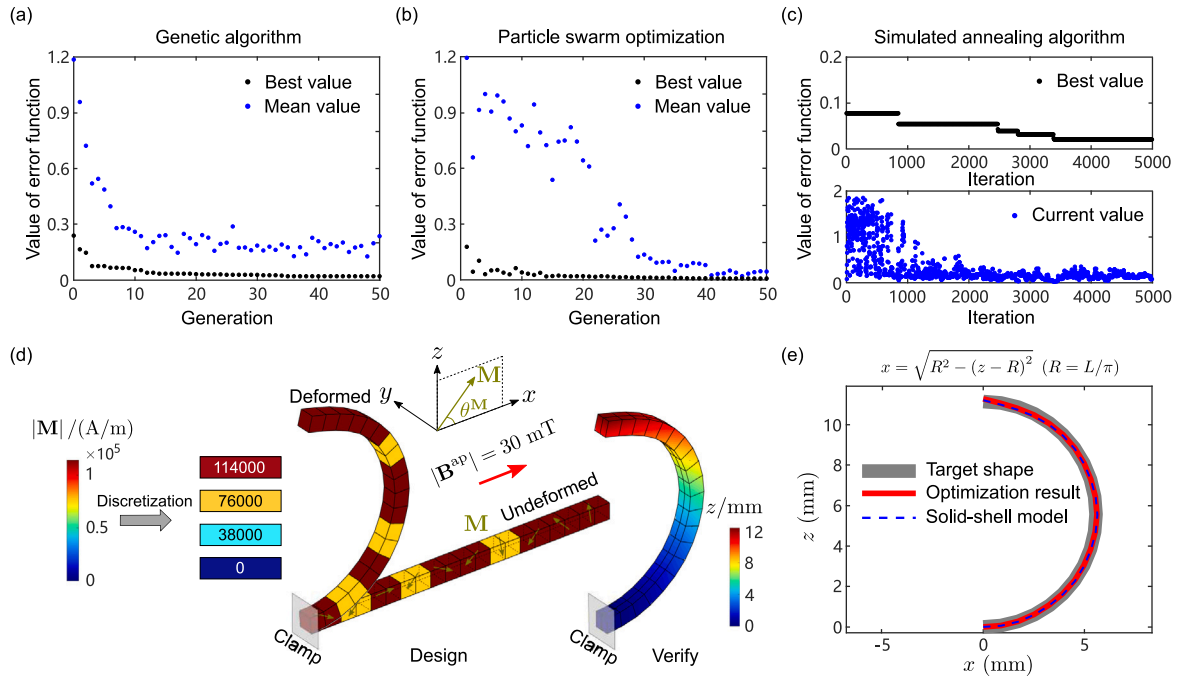

Fig. 5. A hard-magnetic beam deforms into the target shape $x = \sqrt{R^2 - (z-R)^2}$, where $R = L/\pi$ under the excitation of applied magnetic field $\mathbf{B}^{\text{ap}} = 30\mathbf{d}_1$ mT. Three intelligent optimization algorithms are used to solve the inverse problem in the mixed domain with magnetization intensity $|\mathbf{M}| = \{0, 38, 76, 114\}$ kA/m and its direction $\theta^{\mathbf{M}} = 0° \sim 360°$. (a) Optimization process of genetic algorithm (GA). (b) Optimization process of particle swarm optimization algorithm (PSO). (c) Optimization process of simulated annealing algorithm (SA). The blue and black dots represent (average) results and optimal solutions of the current generation, respectively. (d) Design of the hard-magnetic beam with minimum error (0.40%) in the optimization results. (e) Comparison of the target shape, optimization result and solid-shell model [41].

can be seen that the optimized result remarkably matches the target shape.

Based on above cases, we can see that the inverse design strategy obtains reliable results with different optimization algorithms. Moreover, it can flexibly change the independent variables under different conditions and can be optimized in continuous, discrete, and hybrid domains. In the process of optimization, these three algorithms have their own advantages and disadvantages. GA can jump out of the local solution but the convergence speed is slow. PSO converges quickly, but it is prone to "precocious" and fall into local rather than optimal solutions. SA has only one individual for iteration and cannot run in parallel.

4.2. Inverse design of hard-magnetic beams with multi-step deformations

We have shown in Section 4.1 that hard-magnetic beams can flexibly program deformations of target shapes (exponential, sinusoidal, and semicircular) with a fixed actuating magnetic field. We next design a swimming robot and a soft gripper consisting of hard-magnetic beams that can make multiple shape changes in response to multi-step actuation of changing magnetic fields. The design strategy adopted for magnetization density $\mathbf{M}$ in this section remain the same as that in Section 4.1.3. The total relative error function is defined as the sum of the relative errors in multiple steps,

$$f\left(\left\{\mathbf{M}^j, \mathbf{B}_1^{\text{ap}}, \ldots, \mathbf{B}_p^{\text{ap}}\right\}\right) = \sum_{k=1}^{p} f\left(\left\{\mathbf{M}^j, \mathbf{B}_k^{\text{ap}}\right\}\right) = \sum_{k=1}^{p} \frac{\sum_{i=1}^{N+1} \left|\left\{\mathbf{x}_{\text{ex}}^i\right\}_k - \left\{\mathbf{x}_{\text{n}}^i\right\}_k\right|}{\sum_{i=1}^{N+1} \left|\left\{\mathbf{x}_{\text{ex}}^i\right\}_k\right|}, \tag{17}$$

where $\mathbf{B}_k^{\text{ap}}$ $(k = 1, \ldots, p)$ represents the applied magnetic field of step k $(k = 1, \ldots, p)$, $\left\{\mathbf{x}_{\text{ex}}^i\right\}_k$ $(i = 1, 2, \ldots, N+1, k = 1, \ldots, p)$ and $\left\{\mathbf{x}_{\text{n}}^i\right\}_k$ $(i = 1, 2, \ldots, N+1, k = 1, \ldots, p)$ represent the node coordinates corresponding to the target and actual shape of the hard-magnetic beam under the current applied magnetic field $\mathbf{B}_k^{\text{ap}}$ of step k, respectively.

Some swimming robots have tentacles that can repeatedly deform and paddle in the liquid under the excitation of external magnetic fields [79,80]. Due to the limited deformation capacity, these tentacles can only swing symmetrically on one or both sides. However, organisms in nature may have asymmetric shapes and their tentacles may have inconsistent amplitudes when swinging back and forth during swimming, as shown in Fig. 6(a). Here, we design a hard-magnetic swimming robot, which consists of a body (non-magnetic region) and four identical tentacles (hard-magnetic beams), as shown in Figs. 6(b) and (d). The tentacles can be transformed into parabolic shapes ($z_1 = 0.05x_1^2$, $z_2 = -0.2x_2^2$) or sine waves ($z_1 = 3\left[1 - \cos\left(0.06\pi x_1\right)\right]$, $z_2 = -6\left[1 - \cos\left(0.07\pi x_2\right)\right]$) (taking the right tentacles as an example and the left side is symmetrical) under the drive of magnetic fields at two steps $\mathbf{B}_1^{\text{ap}}$ and $\mathbf{B}_2^{\text{ap}}$, where the two-step deformation shapes are asymmetric. We consider the tentacle as a cantilever beam with a rectangular cross-section of length $L = 17.5$ mm, width and thickness $W = H = 0.875$ mm. Assuming that the actuating magnetic field is parallel to the z-axis, the variation ranges of applied magnetic fields upon optimization read $|\mathbf{B}_1^{\text{ap}}| = 0 \sim 30$ mT and $|\mathbf{B}_2^{\text{ap}}| = -30 \sim 0$ mT. The optimization results of both tentacles with different deformation shapes are illustrated in Table 4, with minimum errors of 3.52% and 2.85%, respectively. One can see in Figs. 6(c) and (e) that the optimization results effectively achieve the target multi-step deformations.

We next design two hard-magnetic soft grippers composed of five fingers based on the target grasping movement and process of human hands (see Fig. 7). Unlike previous single-step grippers, we notice that the hand needs to go through two processes of opening and gripping from the relaxed state during grasping, as illustrated in Fig. 7(a). Figs. 7(b) and (d) show two types of hard-magnetic soft grippers. Five programmed hard-magnetic beams act as "fingers", which can be transformed into the sine wave $z_1 = 5.69\sin\left(0.0306\pi x_1\right)$ or quarter circle shape $z_1 = \sqrt{R_1^2 - \left(x_1 - R_1\right)^2}$, where $R_1 = 2L/\pi$ under the magnetic

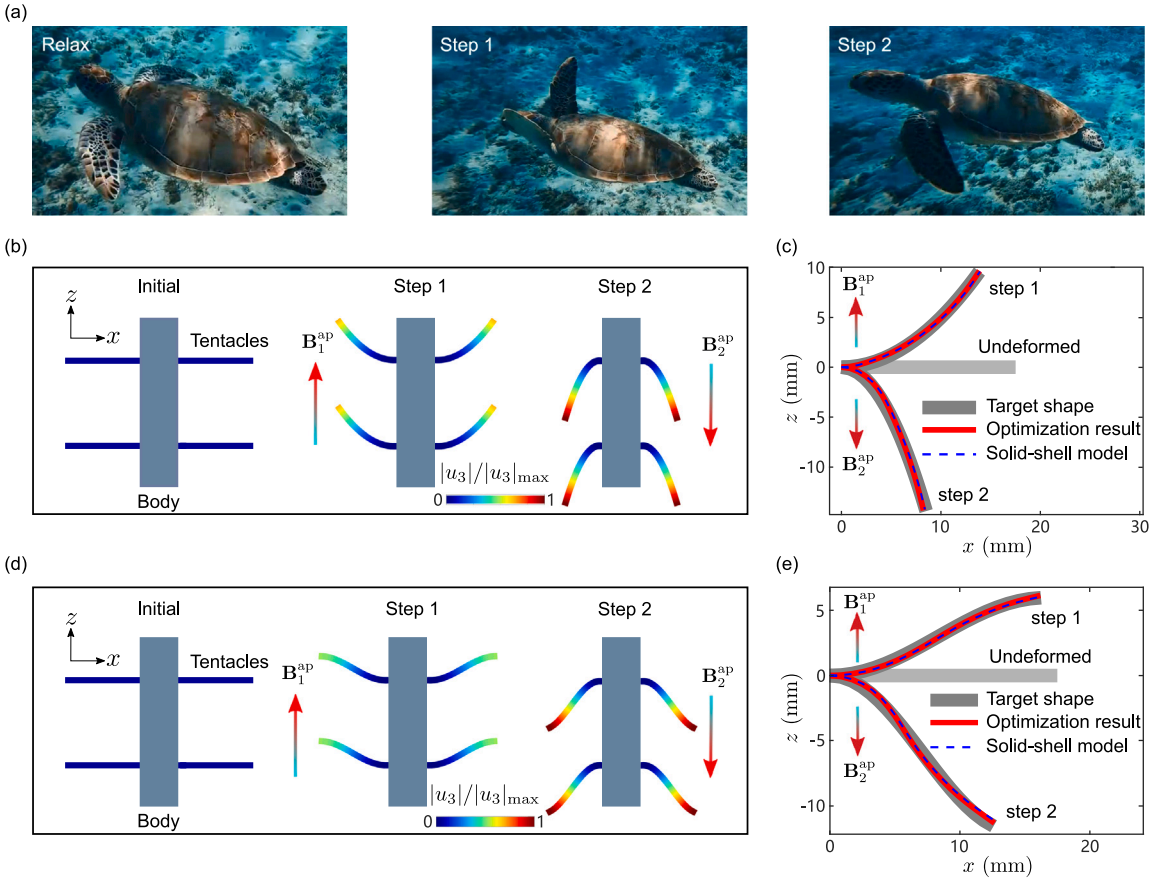

Fig. 6. Multi-step hard-magnetic swimming robot. (a) The swimming process of a sea turtle on the seabed. (b), (d) Motion designs of two kinds of hard-magnetic swimming robots, whose tentacles can deform into parabolic shapes ($z_1 = 0.05x_1^2$, $z_2 = -0.2x_2^2$) or sine waves ($z_1 = 3\left[1-\cos\left(0.06\pi x_1\right)\right]$, $z_2 = -6\left[1-\cos\left(0.07\pi x_2\right)\right]$) under the actuation of magnetic fields at two steps $\mathbf{B}_1^{\text{ap}}$ and $\mathbf{B}_2^{\text{ap}}$. (c), (e) Comparison of the target shape, optimization result and solid-shell model [41].

Table 5
Each finger of the hard-magnetic soft gripper can deform into the sine wave $z_1 = 5.69\sin\left(0.0306\pi x_1\right)$ or quarter circle shape $z_1 = \sqrt{R_1^2 - \left(x_1 - R_1\right)^2}$, where $R_1 = 2L/\pi$ under the magnetic field $\mathbf{B}_1^{\text{ap}}$, and then into the semi-circle shape $z_2 = \sqrt{R_2^2 - \left(x_2 - R_2\right)^2}$, where $R_2 = L/\pi$ under the magnetic field $\mathbf{B}_2^{\text{ap}}$. Distributions of magnetic density $\mathbf{M}$ and two-step applied magnetic field are calculated iteratively by three intelligent optimization algorithms in the mixed domain with magnetization intensity $|\mathbf{M}|$ ={0, 38, 76, 114} kA/m, its direction $\theta^{\mathbf{M}} = 0° \sim 360°$, and applied magnetic fields $|\mathbf{B}_1^{\text{ap}}| = 0 \sim 100$ mT and $|\mathbf{B}_2^{\text{ap}}| = 0 \sim 100$ mT.

Shape	Algorithm	Element	1(2)	3(4)	5(6)	7(8)	9(10)	11(12)	13(14)	15(16)	17(18)	19(20)	$\lvert\mathbf{B}_1^{\text{ap}}\rvert$(mT)	$\lvert\mathbf{B}_2^{\text{ap}}\rvert$(mT)	Error(%)
Case 1	GA	$\lvert\mathbf{M}\rvert$ (kA/m)	76	114	114	76	76	76	76	76	38	38	20.6	74.4	6.35
		$\theta^{\mathbf{M}}$ (°)	229.8	212.4	306.6	336.5	51.8	292.3	31.6	185.3	14.0	197.3			
	PSO	$\lvert\mathbf{M}\rvert$ (kA/m)	114	76	76	0	76	38	0	38	38	38	19.0	90.7	7.01
		$\theta^{\mathbf{M}}$ (°)	246.3	263.4	302.8	0	322.3	77.6	0	38.8	273.2	148.8			
	SA	$\lvert\mathbf{M}\rvert$ (kA/m)	114	114	76	114	0	38	0	0	38	38	15.4	89.4	6.17
		$\theta^{\mathbf{M}}$ (°)	227.6	265.9	284.7	335.1	0	19.9	0	0	189.5	30.6			
Case 2	GA	$\lvert\mathbf{M}\rvert$ (kA/m)	114	76	38	76	0	0	38	0	76	76	4.0	17.7	2.91
		$\theta^{\mathbf{M}}$ (°)	30.5	176.4	24.6	19.5	0	0	303.5	0	265.3	278.6			
	PSO	$\lvert\mathbf{M}\rvert$ (kA/m)	0	0	0	0	114	114	114	114	0	114	3.4	12.2	1.74
		$\theta^{\mathbf{M}}$ (°)	0	0	0	0	355.2	81.8	234.3	295.3	0	263.3			
	SA	$\lvert\mathbf{M}\rvert$ (kA/m)	38	76	0	0	0	38	0	114	114	0	3.5	36.8	3.82
		$\theta^{\mathbf{M}}$ (°)	121.8	44.5	0	0	0	26.8	0	316.4	251.4	0			

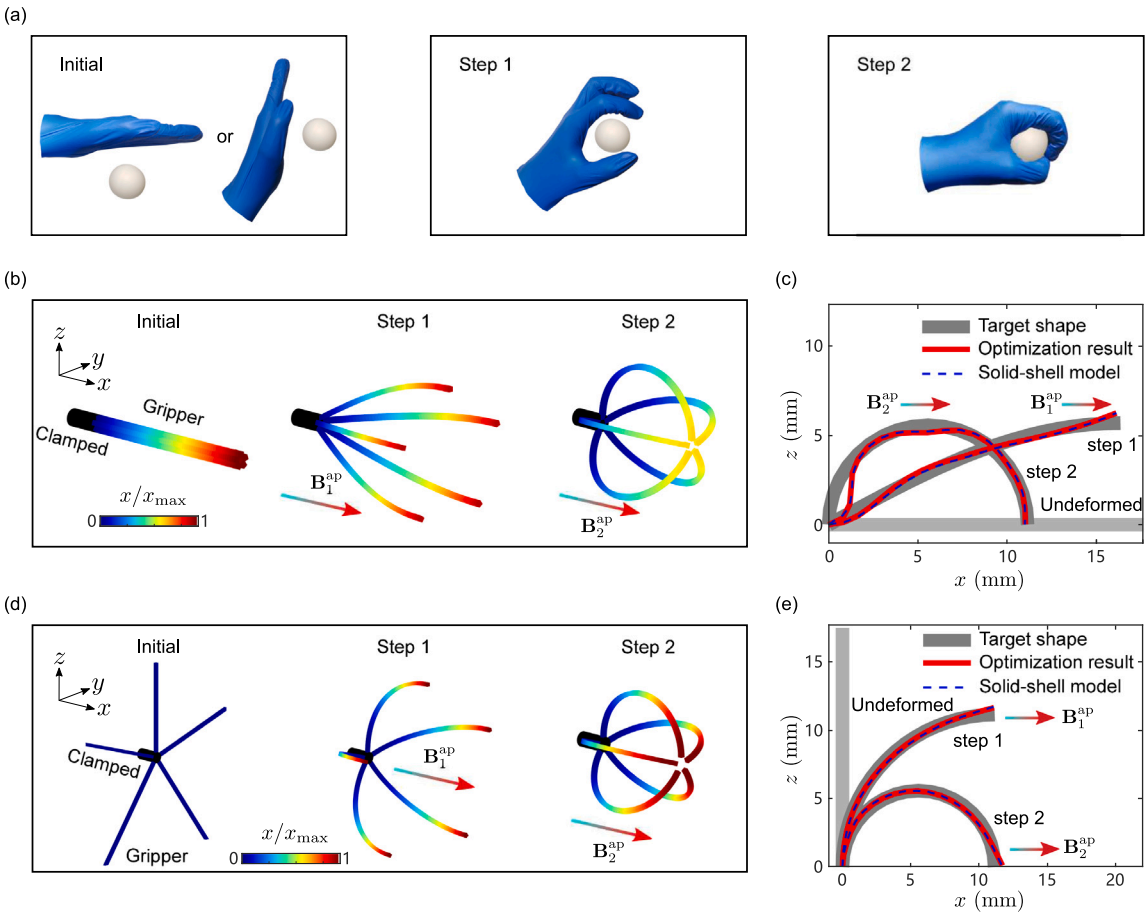

Fig. 7. Multi-step hard-magnetic soft gripper. (a) The grasping process of the hand. (b), (d) Deformation designs of two kinds of hard-magnetic soft grippers, with five identical hard-magnetic beams arranged symmetrically along the ring. Each beam can deform into the sine wave $z_1 = 5.69\sin(0.0306\pi x_1)$ or quarter circle shape $z_1 = \sqrt{R_1^2 - (x_1 - R_1)^2}$, where $R_1 = 2L/\pi$ under the magnetic field $\mathbf{B}_1^{\mathrm{ap}}$, and then into the semi-circle shape $z_2 = \sqrt{R_2^2 - (x_2 - R_2)^2}$, where $R_2 = L/\pi$ under the magnetic field $\mathbf{B}_2^{\mathrm{ap}}$. (c), (e) Comparison of the target shape, optimization result and solid-shell model [41].

field of $\mathbf{B}_1^{\mathrm{ap}}$, and then into the semi-circle shape $z_2 = \sqrt{R_2^2 - (x_2 - R_2)^2}$, where $R_2 = L/\pi$ under the magnetic field of $\mathbf{B}_2^{\mathrm{ap}}$. With these "fingers", the gripper can perform the grasping process of opening and grip from the relaxed state. We consider the "finger" as a cantilever beam with a rectangular cross-section of length $L = 17.5$ mm, width and thickness $W = H = 0.4375$ mm. Considering that the actuating magnetic field is parallel to the x-axis, the variation ranges of applied magnetic fields during optimization read $|\mathbf{B}_1^{\mathrm{ap}}| = 0 \sim 100$ mT and $|\mathbf{B}_2^{\mathrm{ap}}| = 0 \sim 100$ mT. The optimization results of both grippers with different deformation shapes are shown in Table 5, with minimum errors of 6.17% and 1.74%, respectively. As shown in Fig. 7(c), the error at the fixed end of the first type of gripper is observable, since the deformation at the boundary cannot be precisely introduced in the design, but it does not affect the grasping function.

4.3. Inverse design of thin-walled network structures

We now program the chiral deformation of hard-magnetic network structure so that the entire structure can reach the target shape driven by an applied magnetic field, as shown in Fig. 8(a). Selective particle trapping can be achieved by exploiting spatial variations in regions within the deformed network structure [33]. We divide the network structure into four types by classifying the local deformations (see Fig. 8(b)). Let us assume that four hard-magnetic beams transform into the target shapes ($z_1 = -3\sin(0.062\pi x_1)$, $z_2 = 3\sin(0.062\pi x_2)$, $x_3 = -3\sin(0.062\pi z_3)$, $x_4 = 3\sin(0.062\pi z_4)$) under the magnetic field $\mathbf{B}^{\mathrm{ap}} = 30\mathbf{d}_3$ mT. The geometric parameters of the hard-magnetic beam are set as length $L = 17.5$ mm, width $W = L/2 = 8.75$ mm and thickness $H = L/20 = 0.875$ mm. The magnetization density $\mathbf{M}$ varies in the xz plane and is chosen in the discrete domain {0, 38, 76, 114} kA/m, while the direction parameter $\theta^{\mathbf{M}}$ varies in the continuous domain $0° \sim 360°$. The optimization results of four hard-magnetic beams with different deformations are listed in Table 6, with minimum errors of 0.95%, 1.00%, 1.10% and 1.12%, respectively. The computational results of the hard-magnetic network structure at magnetic fields $|\mathbf{B}^{\mathrm{ap}}| = 50, 100, 150$ and 200 mT when using the optimized magnetization distribution are shown in Fig. 8(d). It can be seen that the hard-magnetic network structure can effectively achieve the target shape.

5. Concluding remarks

We have proposed an inverse design strategy for programmable deformations of hard-magnetic soft materials and structures. We have established a functional relation between the deformed shape and its magnetization density and external magnetic field using a 3D hard-magnetic rod model, which transforms the inverse problem of the bending deformation into a highly nonlinear and non-derivable function extremum problem that can be solved by intelligent optimization algorithms. This novel approach enables hard-magnetic beams to achieve precise, desired deformations through the strategic design of material magnetization densities and external magnetic fields.

Based on our inverse design strategy, we have explored shape changes of hard-magnetic beams under three different magnetization

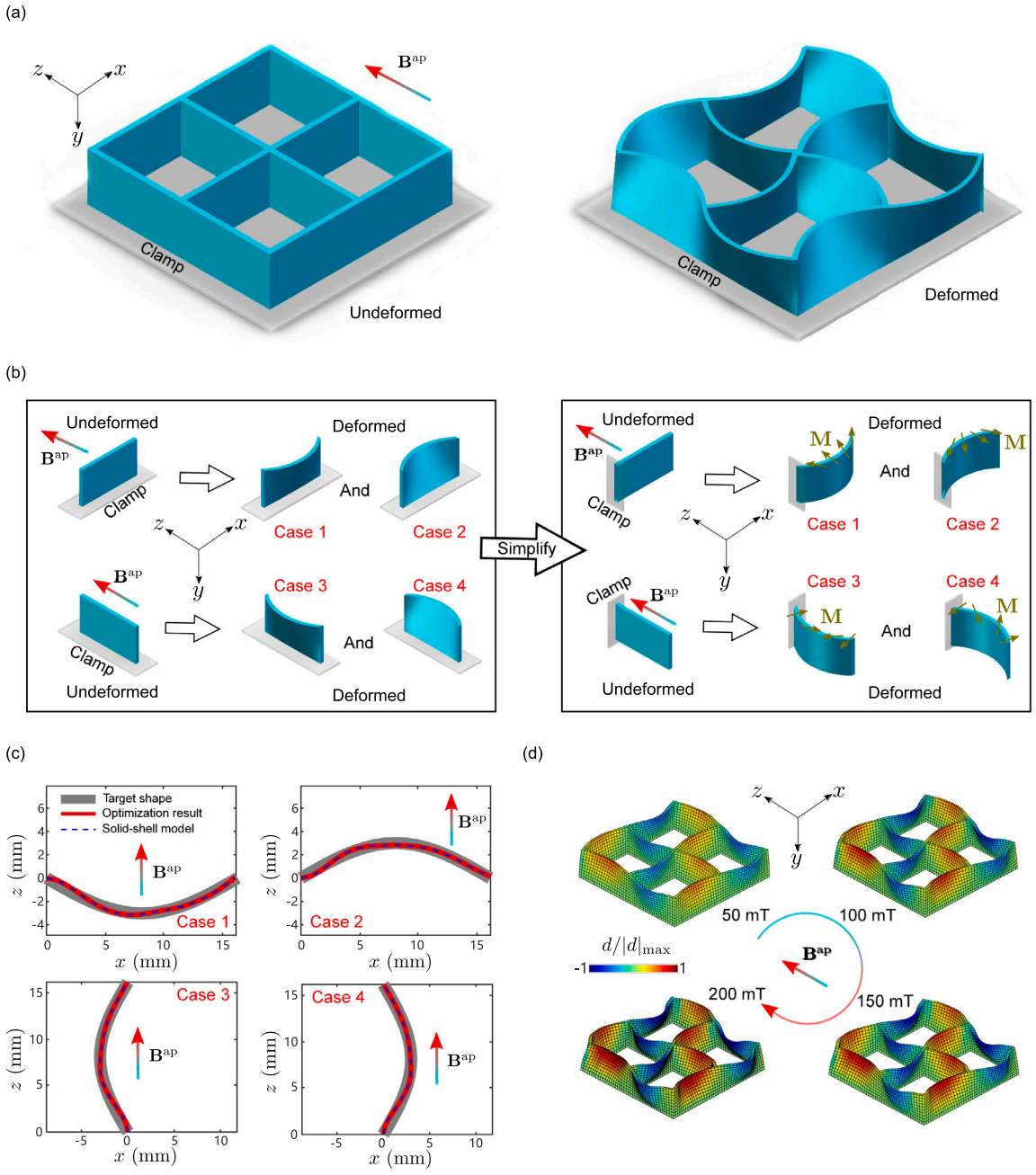

Fig. 8. Hard-magnetic network structure. (a) Chiral deformation of a hard-magnetic network structure under magnetic field $\mathbf{B}^{\mathrm{ap}}$. (b) The hard-magnetic network structure is divided into hard-magnetic beams with four different deformation modes. (c) Comparison of the target shapes ($z_1 = -3\sin\left(0.062\pi x_1\right)$, $z_2 = 3\sin\left(0.062\pi x_2\right)$, $x_3 = -3\sin\left(0.062\pi z_3\right)$, $x_4 = 3\sin\left(0.062\pi z_4\right)$), optimization result and solid-shell model [41]. (d) Numerical results of the hard-magnetic network structure at magnetic fields $|\mathbf{B}^{\mathrm{ap}}| = 50, 100, 150$ and 200 mT using the optimized magnetization distribution, where color bar $d = x$ ($|u_1| > |u_3|$) or $d = z$ ($|u_1| \leq |u_3|$).

Table 6
Four hard-magnetic beams deform into the target shapes ($z_1 = -3\sin(0.062\pi x_1)$, $z_2 = 3\sin(0.062\pi x_2)$, $x_3 = -3\sin(0.062\pi z_3)$, $x_4 = 3\sin(0.062\pi z_4)$) under the excitation of applied magnetic field $\mathbf{B}^{ap} = 30\mathbf{d}_3$ mT. Distributions of magnetic density $\mathbf{M}$ is calculated iteratively by three intelligent optimization algorithms in the mixed domain with magnetization intensity $|\mathbf{M}|$ ={0, 38, 76, 114} kA/m and its direction $\theta^{\mathbf{M}} = 0° \sim 360°$.

Shape	Algorithm	Element	1(2)	3(4)	5(6)	7(8)	9(10)	11(12)	13(14)	15(16)	17(18)	19(20)	Error (%)
Case 1	GA	$\|\mathbf{M}\|$ (kA/m)	114	38	38	38	76	114	76	114	38	38	2.08
		$\theta^{\mathbf{M}}$ (°)	182.8	216.8	181.4	274.2	88.8	44.8	136.4	53.7	98.7	343.7	
	PSO	$\|\mathbf{M}\|$ (kA/m)	114	114	114	76	0	38	38	76	38	38	0.95
		$\theta^{\mathbf{M}}$ (°)	183.6	182.6	102.6	100.4	0	84.2	73.9	66.7	55.5	32.7	
	SA	$\|\mathbf{M}\|$ (kA/m)	114	76	38	76	76	76	38	114	38	0	1.05
		$\theta^{\mathbf{M}}$ (°)	210.7	169.8	147.0	104.7	69.5	104.8	60.1	59.4	48.2	0	
Case 2	GA	$\|\mathbf{M}\|$ (kA/m)	114	114	38	114	0	114	0	76	76	76	1.32
		$\theta^{\mathbf{M}}$ (°)	345.8	16.1	346.4	109.5	0	84.7	0	115.4	150.6	102.7	
	PSO	$\|\mathbf{M}\|$ (kA/m)	114	76	114	0	0	76	76	38	76	38	1.00
		$\theta^{\mathbf{M}}$ (°)	328.2	298.1	64.4	0	0	109.2	94.5	109.7	141.7	114.4	
	SA	$\|\mathbf{M}\|$ (kA/m)	114	114	0	76	114	38	0	76	38	38	1.06
		$\theta^{\mathbf{M}}$ (°)	3.6	19.4	0	68.0	89.7	100.7	0	133.4	87.6	148.2	
Case 3	GA	$\|\mathbf{M}\|$ (kA/m)	114	76	76	76	114	76	38	38	76	38	1.31
		$\theta^{\mathbf{M}}$ (°)	341.9	26.4	41.5	46.5	123.8	78.6	109.3	113.9	133.2	118.6	
	PSO	$\|\mathbf{M}\|$ (kA/m)	114	114	0	114	38	38	38	114	0	0	1.10
		$\theta^{\mathbf{M}}$ (°)	12.2	5.0	0	82.4	102.5	71.6	106.4	130.4	0	0	
	SA	$\|\mathbf{M}\|$ (kA/m)	114	114	0	38	0	0	38	76	76	76	1.77
		$\theta^{\mathbf{M}}$ (°)	317.1	265.7	0	47.2	0	0	131.4	139.6	124.0	98.3	
Case 4	GA	$\|\mathbf{M}\|$ (kA/m)	114	38	114	76	38	76	38	76	0	0	1.32
		$\theta^{\mathbf{M}}$ (°)	181.8	204.1	150.5	76.1	44.9	129.6	325.0	53.8	0	0	
	PSO	$\|\mathbf{M}\|$ (kA/m)	114	76	0	0	76	0	38	0	0	76	1.12
		$\theta^{\mathbf{M}}$ (°)	188.6	173.5	0	0	104.9	0	303.6	0	0	56.1	
	SA	$\|\mathbf{M}\|$ (kA/m)	76	114	0	0	76	0	0	114	0	0	1.55
		$\theta^{\mathbf{M}}$ (°)	179.9	180.4	0	0	81.5	0	0	55.8	0	0	

density programming modes, and compared three intelligent optimization algorithms. All the optimization results remarkably match the target shapes, demonstrating the effectiveness and versatility of our strategy for programmable morphing design. Lastly, we extended our method to more complex optimization cases involving multi-step deformations of hard-magnetic beam networks and cellular thin-walled structures. The results demonstrate not only the powerful programmability of hard-magnetic soft materials, but also the great potential of our strategy for rational inverse design of hard-magnetic robotics and biomimetic devices.

CRediT authorship contribution statement

Maoyuan Li: Writing – original draft, Visualization, Validation, Software, Methodology, Investigation, Formal analysis. **Yifan Yang:** Writing – review & editing, Writing – original draft, Visualization, Validation, Software, Methodology, Investigation, Funding acquisition, Formal analysis. **Ya Wen:** Investigation, Formal analysis. **Jizhai Cui:** Writing – review & editing. **Wei Cheng:** Writing – review & editing. **Enming Song:** Writing – review & editing. **Fan Xu:** Writing – review & editing, Writing – original draft, Validation, Supervision, Resources, Project administration, Methodology, Investigation, Funding acquisition, Formal analysis, Conceptualization.

Declaration of competing interest

The authors declare that they have no known competing financial interests or personal relationships that could have appeared to influence the work reported in this paper.

Acknowledgments

This work is supported by the National Natural Science Foundation of China (Grants No. 12425204, 12122204, and 12372096), Shanghai Pilot Program for Basic Research-Fudan University (Grant No. 21TQ1400100-21TQ010), Shanghai Shuguang Program (Grant No. 21SG05), China Postdoctoral Science Foundation, China (Grant No. 2024M750510), Shanghai Post-doctoral Excellence Program (Grant No. 2023208), and Shanghai Municipal Education Commission (Grant No. 24KXZNA14).

Appendix A. Numerical implementation of 3D hard-magnetic rod model

The co-rotational approach for spatial beam structures is presented here. We focus on a single element with nodes A and B (see Fig. 9), tracked over a time interval between t_a and $t_b = t_a + \Delta t$. Similar to conventional 3D beam elements, the spatial state of AB is fully described by a set of twelve variables associated with the nodes, *i.e.*, position vector $\mathbf{x}_i$ and angle vector $\boldsymbol{\theta}_i$, where $i = A, B$. Based on the known reference state at time t_a, the elongation of AB reads

$$\Delta l = l_b - l_a = |\mathbf{x}_B^b - \mathbf{x}_A^b| - |\mathbf{x}_B^a - \mathbf{x}_A^a|. \tag{18}$$

In the next state t_b, the orientation of AB reads

$$\mathbf{d}_1^b = \frac{\mathbf{x}_B^b - \mathbf{x}_A^b}{|\mathbf{x}_B^b - \mathbf{x}_A^b|}. \tag{19}$$

The rotation of node i from t_a to t_b is defined as $\Delta\boldsymbol{\theta}_i = \boldsymbol{\theta}_i^b - \boldsymbol{\theta}_i^a$. The transformation angle from directors $\mathbf{d}_1^a$ to $\mathbf{d}_1^b$ can be computed as $\theta_{ab} = \sin^{-1}(|\mathbf{d}_1^a \times \mathbf{d}_1^b|)$, while the torsional component at node A is given by the projection $\Delta\hat{\theta}_{Ax} = \Delta\boldsymbol{\theta}_A \cdot \mathbf{d}_1^a$. Subsequently, the rigid-body rotation can be given by

$$\boldsymbol{\gamma} = \Delta\hat{\theta}_{Ax}\mathbf{d}_1^a + \theta_{ab}\frac{\mathbf{d}_1^a \times \mathbf{d}_1^b}{|\mathbf{d}_1^a \times \mathbf{d}_1^b|}. \tag{20}$$

For the spatial rotational transformation, we normalize $\boldsymbol{\gamma}$ to obtain $\mathbf{e}_\gamma = \{l_\gamma, m_\gamma, n_\gamma\}^{\mathrm{T}} = \boldsymbol{\gamma}/|\boldsymbol{\gamma}|$, where the rotation matrix is constructed as [71]

$$\mathbf{R}_\gamma = \mathbf{I} + \sin|\boldsymbol{\gamma}|\mathbf{W}_\gamma + (1 - \cos|\boldsymbol{\gamma}|)\mathbf{W}_\gamma^2,$$
$$\mathbf{W}_\gamma = \begin{bmatrix} 0 & -n_\gamma & m_\gamma \\ n_\gamma & 0 & -l_\gamma \\ -m_\gamma & l_\gamma & 0 \end{bmatrix}. \tag{21}$$

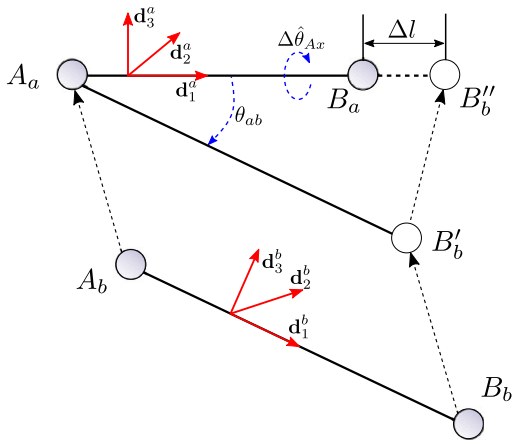

Fig. 9. The displacement and rotation of segment AB between t_a and t_b.

The rotational vector $\boldsymbol{\gamma}$ is expressed in the global coordinate system and can be transformed to the local coordinate at time t_a as $\hat{\boldsymbol{\gamma}} = (\mathbf{Q}^a)^{\mathrm{T}}\boldsymbol{\gamma}$. Here, $\mathbf{Q} = [\mathbf{d}_1, \mathbf{d}_2, \mathbf{d}_3]$ is the transformation matrix, where $\mathbf{d}_1, \mathbf{d}_2$ and $\mathbf{d}_3$ are the corresponding basis vectors. After eliminating the rigid-body rotation, the nodal rotation at node i becomes

$$\Delta\hat{\boldsymbol{\beta}}_i = \Delta\hat{\boldsymbol{\theta}}_i - \hat{\boldsymbol{\gamma}}, \quad i = A, B. \tag{22}$$

Within the local frame at time t_a, both the axial deformation Δu_m and twist angle $\Delta\hat{\beta}_x$ along $\mathbf{d}_1^a$ follow linear interpolation and are defined by $\Delta u_m = \Delta l\xi$ and $\Delta\hat{\beta}_x = \Delta\hat{\beta}_{Bx}\xi$, with $\xi = \hat{x}/l_a$ representing the normalized position in the local coordinate system. Then, the associated axial strain and the rate of twist can be derived as

$$\begin{aligned}\Delta\varepsilon_m &= \frac{\mathrm{d}\Delta u_m}{\mathrm{d}\hat{x}},\\ \Delta\kappa_1 &= \frac{\mathrm{d}\Delta\hat{\beta}_x}{\mathrm{d}\hat{x}}.\end{aligned} \tag{23}$$

To characterize the bending deflection, we employ cubic shape functions similar to classical beam elements. Here, we derive $\Delta\kappa_2$ as a representative case,

$$w = (\xi^3 - 2\xi^2 + \xi)l_a\Delta\hat{\beta}_{Ay} + (\xi^3 - \xi^2)l_a\Delta\hat{\beta}_{By}. \tag{24}$$

The corresponding rotational angle and bending curvature are given by

$$\begin{aligned}\Delta\hat{\beta}_y &= -\frac{\mathrm{d}w}{\mathrm{d}\hat{x}} = \begin{bmatrix}-1 + 4\xi - 3\xi^2 & 2\xi - 3\xi^2\end{bmatrix}\begin{bmatrix}\Delta\hat{\beta}_{Ay}\\ \Delta\hat{\beta}_{By}\end{bmatrix} = \mathbf{N}_b\begin{bmatrix}\Delta\hat{\beta}_{Ay}\\ \Delta\hat{\beta}_{By}\end{bmatrix},\\ \Delta\kappa_2 &= -\frac{\mathrm{d}^2w}{\mathrm{d}\hat{x}^2} = \frac{1}{l_a}\begin{bmatrix}4 - 6\xi & 2 - 6\xi\end{bmatrix}\begin{bmatrix}\Delta\hat{\beta}_{Ay}\\ \Delta\hat{\beta}_{By}\end{bmatrix}.\end{aligned} \tag{25}$$

Following the same derivation approach, one can obtain $\Delta\kappa_3$. Incorporating $\Delta\varepsilon_m$ and $\Delta\kappa_i$ $(i = 1, 2, 3)$ into Eq. (5) yields the incremental variables $\Delta\hat{\mathbf{f}}_i^{\mathrm{el}}$ and $\Delta\hat{\mathbf{m}}_i^{\mathrm{el}}$ at the nodes $i = A, B$. The total elastic forces of node i in state t_b are then updated through $\hat{\mathbf{f}}_i^{\mathrm{el}(b)} = \hat{\mathbf{f}}_i^{\mathrm{el}(a)} + \Delta\hat{\mathbf{f}}_i^{\mathrm{el}}$. The expression for the moments $\hat{\mathbf{m}}_i^{\mathrm{el}(b)}$ follows a similar form. Moreover, magnetic contributions $\hat{\mathbf{f}}_i^{\mathrm{ma}}$ and $\hat{\mathbf{m}}_i^{\mathrm{ma}}$ $(i = A, B)$ are computed using Eq. (13). Detailed formulations can be found in Yang et al. [49].

The internal forces $\hat{\mathbf{f}}_i^{\mathrm{int}}$ and moments $\hat{\mathbf{m}}_i^{\mathrm{int}}$ of node i comprise both elastic and magnetic part, expressed as $\hat{\mathbf{f}}_i^{\mathrm{int}} = \hat{\mathbf{f}}_i^{\mathrm{el}(b)} + \hat{\mathbf{f}}_i^{\mathrm{ma}}$ and $\hat{\mathbf{m}}_i^{\mathrm{int}} = \hat{\mathbf{m}}_i^{\mathrm{el}(b)} + \hat{\mathbf{m}}_i^{\mathrm{ma}}$, $i = A, B$. Finally, transforming the above variables to the global coordinate system gives

$$\begin{aligned}\mathbf{f}_i^{\mathrm{int}} &= \mathbf{R}_\gamma\mathbf{Q}^a\hat{\mathbf{f}}_i^{\mathrm{int}},\\ \mathbf{m}_i^{\mathrm{int}} &= \mathbf{R}_\gamma\mathbf{Q}^a\hat{\mathbf{m}}_i^{\mathrm{int}}.\end{aligned} \tag{26}$$

The numerical solution of the nonlinear system employs an explicit time integration scheme, which offers computational advantages with parallelization. The temporal domain is subdivided into n discrete intervals with a size of Δt. All state variables at the next step t_{i+1} can be computed solely from the previous step t_i. Following Newton's equations of motion, the nodal variables $\mathbf{x}$ and $\boldsymbol{\theta}$ are governed by

$$\begin{aligned}m_\alpha\ddot{\mathbf{x}}_\alpha &= \mathbf{f}_\alpha,\\ \mathbf{J}_\alpha\ddot{\boldsymbol{\theta}}_\alpha &= \mathbf{m}_\alpha,\end{aligned} \tag{27}$$

in which the index α is used to identify the node, with m_α and $\mathbf{J}_\alpha$ representing its associated lumped mass and moment of inertia tensor, respectively. The total nodal force $\mathbf{f}_\alpha$ and moment $\mathbf{m}_\alpha$ at node α consist of three distinct components, given by

$$\begin{aligned}\mathbf{f}_\alpha &= \mathbf{f}_\alpha^{\mathrm{ext}} - \mathbf{f}_\alpha^{\mathrm{int}} - \mathbf{f}_\alpha^{\mathrm{dmp}},\\ \mathbf{m}_\alpha &= \mathbf{m}_\alpha^{\mathrm{ext}} - \mathbf{m}_\alpha^{\mathrm{int}} - \mathbf{m}_\alpha^{\mathrm{dmp}}.\end{aligned} \tag{28}$$

Note that the dissipative terms are proportional to velocities, with damping coefficient ζ scaling both translational and rotational components $\mathbf{f}_\alpha^{\mathrm{dmp}} = \zeta\dot{\mathbf{x}}_\alpha$ and $\mathbf{m}_\alpha^{\mathrm{dmp}} = \zeta\dot{\boldsymbol{\theta}}_\alpha$. Here, quasi-static processes are considered. Therefore, mass and damping factors are implemented as computational parameters, which only affect the stability and convergence speed of the solving procedure, but not accuracy. For high-speed transient analysis, viscoelastic effects need to be introduced [81]. For each node α, $\mathbf{f}_\alpha^{\mathrm{int}}$ and $\mathbf{m}_\alpha^{\mathrm{int}}$ are accumulated from its N neighboring elements according to

$$\begin{aligned}\mathbf{f}_\alpha^{\mathrm{int}} &= \sum_{i=1}^{N}\mathbf{f}_{\alpha(i)}^{\mathrm{int}},\\ \mathbf{m}_\alpha^{\mathrm{int}} &= \sum_{i=1}^{N}\mathbf{m}_{\alpha(i)}^{\mathrm{int}}.\end{aligned} \tag{29}$$

For the time derivative in Eq. (27), we employ the central difference method [72], where the temporal discretization for the step $n+1$ reads

$$\begin{aligned}\mathbf{x}_\alpha^{n+1} &= \frac{\Delta t^2}{m_a}\mathbf{f}_\alpha^n + 2\mathbf{x}_\alpha^n - \mathbf{x}_\alpha^{n-1},\\ \boldsymbol{\theta}_\alpha^{n+1} &= \Delta t^2\mathbf{J}_\alpha^{-1}\mathbf{m}_\alpha^n + 2\boldsymbol{\theta}_\alpha^n - \boldsymbol{\theta}_\alpha^{n-1}, \quad (n = 0, 1, 2\ldots).\end{aligned} \tag{30}$$

Appendix B. Intelligent optimization algorithms

In this section, we provide a brief introduction to three intelligent algorithms including genetic algorithm, particle swarm optimization, and simulated annealing algorithm. Besides, we present the parameters used in the implementation of these algorithms.

B.1. Genetic algorithm

The genetic algorithm (GA) is a global search optimization algorithm formed by simulating the process of biological heredity and evolution, which belongs to the evolutionary algorithm (EA). GA was first proposed by Holland in the United States and was concluded by Goldberg based on a series of works. Through continuous development, GA has been widely used in machine learning, neural networks, control system optimization and other fields [82–84]. The core of GA is to pass the genetic information of the parent population on to the next generation through the genetic operation of "selection", "crossover" and "mutation". "Selection" is to select some excellent individuals from the parent population according to the individual fitness and directly carry them to the next generation population. The "selection" operation ensures that the excellent genes in the parent population can be preserved. Common selection methods include roulette selection, championship selection, etc. "Crossover" is the selection of some individuals in the paternal generation to exchange part of their chromosomes with crossover probability P_c to produce new individuals. "Crossover" allows offspring to inherit good genes from both parents, which makes it possible to produce better-performing offspring. The design of the crossing needs to be assisted by the coding operation.

Common crossing methods include single-point crossing, multi-point crossing, shuffle crossing, etc. "Mutation" means that an individual in the parent population changes a gene on the chromosome with mutation probability P_m. "Mutation" can maintain the diversity of the population and is conducive to exploring new possible solutions. In this paper, we adopt roulette selection, single-point crossing with crossover probability $P_c = 0.8$ and mutation probability $P_m = 0.01$.

B.2. Particle swarm optimization

The particle swarm optimization (PSO) is a global search optimization algorithm that simulates the foraging migration and flock behavior of birds (population), which belongs to the swarm intelligence algorithm (SI). PSO was first proposed by Kennedy and Eberhart. Because of its simple parameters and strong global search ability, PSO has been widely used in neural network training, fuzzy control and other fields [85–87]. Compared with GA, PSO retains the global search strategy based on populations but adopts the speed-displacement update model to avoid the complex genetic operation (selection, crossover, and mutation) on individuals. Assuming that there is a population composed of N particles and the search is in a D-dimensional space, the update formula of speed $\mathbf{V}_i^t$ and displacement $\mathbf{X}_i^t$ of the ith particle when iterating to generation t reads

$$\begin{aligned}\mathbf{V}_i^{t+1} &= \omega \mathbf{V}_i^t + c_1 r_1^t \left[\left(\mathbf{p}_{\text{best}}\right)_i^t - \mathbf{X}_i^t \right] + c_2 r_2^t \left(\mathbf{g}_{\text{best}}^t - \mathbf{X}_i^t \right), \\ \mathbf{X}_i^{t+1} &= \mathbf{X}_i^t + \mathbf{V}_i^t,\end{aligned} \tag{31}$$

where $\left(\mathbf{p}_{\text{best}}\right)_i^t$ and $\mathbf{g}_{\text{best}}^t$ represent the optimal position of the ith particle and the whole particle swarm when iterating to generation t, respectively. They are called "individual extreme value" and "global extreme value". Parameters r_1^t and r_2^t are uniform random numbers in the range of $[0, 1]$ when iterating to generation t. Parameters c_1 and c_2 are "individual" and "social" learning factors, respectively. In this paper, $c_1 = c_2 = 2$ is taken in the calculation to ensure that individual and group experiences occupy the same proportion. Parameter ω is the inertia weight, which can control the development and exploration ability of the algorithm. We adopt the linear decline strategy to dynamically adjust ω during the search process

$$\omega = \omega_{\max} - \frac{\left(\omega_{\max} - \omega_{\min}\right) t}{T_{\max}}, \tag{32}$$

where $T_{\max}$ represents the maximum number of iterations, and $\omega_{\min}$ and $\omega_{\max}$ are the minimum and maximum inertia weights, respectively. Here, $\omega_{\max} = 0.9$ and $\omega_{\min} = 0.4$ are taken. Under these conditions, ω is large in the initial stage of search so particles can be searched globally in a large range. In the later stage of search, the smaller ω can ensure the fine search of particles near the extreme point, which balances the ability of global search and local search of the algorithm.

B.3. Simulated annealing algorithm

The simulated annealing algorithm (SA) is a global search algorithm formed by simulating the annealing process of solid substances in physics. The idea of SA was first proposed by Metropolis et al. and then Kirkpatrick applied SA to solve combinatorial optimization problems. Nowadays, SA has been widely used in control engineering, structure optimization, machine learning and other fields [88–90]. The core idea of SA comes from the process of solid annealing. Firstly, set a higher initial temperature T_0 (heating process), and then go through the isothermal and cooling process in the iterative process, so that the solution gradually approaches the optimal solution. Unlike GA and PSO, SA has only one individual in the iterative calculation. Assuming that the fitness of solution S_1 is f_1, the way to generate new solution S_2 is

$$S_2 = S_1 + r \times T, \tag{33}$$

where the parameter T represents the current temperature and r is a uniform random number in the range of $[-1, 1]$. The fitness of solution S_2 is f_2, and the increment $\Delta f = f_2 - f_1$. Then accepting the new solution follows Metropolis criteria,

$$p\left(S_1 \to S_2\right) = \begin{cases} 1, & \Delta f < 0, \\ \mathrm{e}^{-\frac{\Delta f}{T}}, & \Delta f \geq 0. \end{cases} \tag{34}$$

It can be seen that even if the fitness of a new solution becomes larger, it can still be accepted. Moreover, the probability of a new solution being accepted is controlled by temperature T. The temperature T is high at the early stage of iteration, and thus the probability of accepting the inferior solution is large, which ensures a large range of global searches. The temperature T remains relatively low at the later stage of the iteration, so only the better solution is accepted, ensuring a finer search near the extreme value. This is very similar to the inertia weight ω in PSO. The temperature remains constant during the isothermal process (inner cycle), and the number of iterations during the isothermal process is called Markov chain length L_a. The temperature T becomes smaller in the cooling process (external cycle). The most commonly used temperature updating function is the exponential regression function,

$$T = 0.95^k \times T_0, \tag{35}$$

where k represents the number of current iterations. In this paper, we set the initial temperature $T_0 = 200$ and Markov chain length $L_a = 100$.

Data availability

Data will be made available on request.

References

[1] Wang Y, Sun J, Liao W, Yang Z. Liquid crystal elastomer twist fibers toward rotating microengines. Adv Mater 2022;34:2107840.
[2] Saed MO, Gablier A, Terentjev EM. Exchangeable liquid crystalline elastomers and their applications. Chem Rev 2021;122:4927–45.
[3] Yang Y, Zhao S, Dai Z, Xu F. Programmable wrinkling patterns of liquid crystal network bilayers on compliant substrates. Int J Solids Struct 2025;309:113206.
[4] Lin W, Kluzek M, Iuster N, Shimoni E, Kampf N, Goldberg R, et al. Cartilage-inspired, lipid-based boundary-lubricated hydrogels. Science 2020;370:335–8.
[5] Heiden A, Preninger D, Lehner L, Baumgartner M, Drack M, Woritzka E, et al. 3D printing of resilient biogels for omnidirectional and exteroceptive soft actuators. Sci Robot 2022;7:eabk2119.
[6] Kim Y, Yuk H, Zhao R, Chester SA, Zhao X. Printing ferromagnetic domains for untethered fast-transforming soft materials. Nature 2018;558:274–9.
[7] Hu W, Lum GZ, Mastrangeli M, Sitti M. Small-scale soft-bodied robot with multimodal locomotion. Nature 2018;554:81–5.
[8] Zhang W, Wang H, Wang H, Chan JYE, Liu H, Zhang B, et al. Structural multicolour invisible inks with submicron 4D printing of shape memory polymers. Nat Commun 2021a;12:112.
[9] Spiegel CA, Hackner M, Bothe VP, Spatz JP, Blasco E. 4D printing of shape memory polymers: From macro to micro. Adv Funct Mater 2022;32:2110580.
[10] Zhao Y, Gao S, Zhang X, Huo W, Xu H, Chen C, et al. Fully flexible electromagnetic vibration sensors with annular field confinement origami magnetic membranes. Adv Funct Mater 2020;30:2001553.
[11] Qi Z, Zhou M, Li Y, Xia Z, Huo W, Huang X. Reconfigurable flexible electronics driven by origami magnetic membranes. Adv Mater Technol 2021;6:2001124.
[12] Ze Q, Wu S, Nishikawa J, Dai J, Sun Y, Leanza S, et al. Soft robotic origami crawler. Sci Adv 2022;8:eabm7834.
[13] Zhang J, Ren Z, Hu W, Soon RH, Yasa IC, Liu Z, et al. Voxelated three-dimensional miniature magnetic soft machines via multimaterial heterogeneous assembly. Sci Robot 2021b;6:eabf0112.
[14] Alam Z, Padmanabhan S, Sharma AK. Magnetically tunable longitudinal wave band gaps in hard-magnetic soft laminates. Int J Mech Sci 2023;249:108262.
[15] Alam Z, Sharma AK. Topology optimization of hard-magnetic soft phononic structures for wide magnetically tunable band gaps. J Appl Mech 2024;91:101009.
[16] Padmanabhan S, Alam Z, Sharma AK. Tunable anti-plane wave bandgaps in 2D periodic hard-magnetic soft composites. Int J Mech Sci 2024;261:108686.
[17] Zhang Q, Rudykh S. Magnetically tunable topological states in translational-rotational coupling metamaterials. Int J Mech Sci 2025;285:109826.

[18] Sharma D, Sharma AK. Dynamic modeling and analysis of viscoelastic hard-magnetic soft actuators with thermal effects. Int J Non-Linear Mech 2024;165:104801.
[19] Kim Y, Parada GA, Liu S, Zhao X. Ferromagnetic soft continuum robots. Sci Robot 2019;4:eaax7329.
[20] Wang L, Zheng D, Harker P, Patel AB, Guo CF, Zhao X. Evolutionary design of magnetic soft continuum robots. Proc Natl Acad Sci USA 2021;118:e2021922118.
[21] Lu L, Sim J, Zhao RR. Mechanics of hard-magnetic soft materials: A review. Mech Mater 2024;189:104874.
[22] Narayanan P, Pramanik R, Arockiarajan A. Hard magnetics and soft materials–a synergy. Smart Mater Struct 2024;33:043001.
[23] Bastola AK, Hossain M. The shape–morphing performance of magnetoactive soft materials. Mater Des 2021;211:110172.
[24] Lucarini S, Hossain M, Garcia-Gonzalez D. Recent advances in hard-magnetic soft composites: Synthesis, characterisation, computational modelling, and applications. Compos Struct 2022;279:114800.
[25] Wu S, Hu W, Ze Q, Sitti M, Zhao R. Multifunctional magnetic soft composites: A review. Multifunct Mater 2020;3:042003.
[26] Chen W, Wang L. Theoretical modeling and exact solution for extreme bending deformation of hard-magnetic soft beams. J Appl Mech 2020;87:041002.
[27] Kuang X, Wu S, Ze Q, Yue L, Jin Y, Montgomery SM, et al. Magnetic dynamic polymers for modular assembling and reconfigurable morphing architectures. Adv Mater 2021;33:2102113.
[28] Lum GZ, Ye Z, Dong X, Marvi H, Erin O, Hu W, et al. Shape-programmable magnetic soft matter. Proc Natl Acad Sci USA 2016;113:E6007–15.
[29] Xu T, Zhang J, Salehizadeh M, Onaizah O, Diller E. Millimeter-scale flexible robots with programmable three-dimensional magnetization and motions. Sci Robot 2019;4:eaav4494.
[30] Deng H, Sattari K, Xie Y, Liao P, Yan Z, Lin J. Laser reprogramming magnetic anisotropy in soft composites for reconfigurable 3D shaping. Nat Commun 2020;11:6325.
[31] Wu S, Hamel CM, Ze Q, Yang F, Qi HJ, Zhao R. Evolutionary algorithm-guided voxel-encoding printing of functional hard-magnetic soft active materials. Adv Intell Syst 2020;2:2000060.
[32] Qi S, Guo H, Fu J, Xie Y, Zhu M, Yu M. 3D printed shape-programmable magneto-active soft matter for biomimetic applications. Compos Sci Technol 2020;188:107973.
[33] Xia N, Jin D, Pan C, Zhang J, Yang Z, Su L, et al. Dynamic morphological transformations in soft architected materials via buckling instability encoded heterogeneous magnetization. Nat Commun 2022;13:7514.
[34] Li X, Zhang D, Wang H, Yang R, Yuan H. Shape-programmable hard-magnetic soft actuators with high magnetic particle content via digital light processing method. Compos Part A Appl Sci Manuf 2025;188:108554.
[35] Zhao R, Kim Y, Chester SA, Sharma P, Zhao X. Mechanics of hard-magnetic soft materials. J Mech Phys Solids 2019;124:244–63.
[36] Garcia-Gonzalez D. Magneto-visco-hyperelasticity for hard-magnetic soft materials: theory and numerical applications. Smart Mater Struct 2019;28:085020.
[37] Dadgar-Rad F, Hossain M. Finite deformation analysis of hard-magnetic soft materials based on micropolar continuum theory. Int J Solids Struct 2022a;251:111747.
[38] Dadgar-Rad F, Hossain M. A micropolar shell model for hard-magnetic soft materials. Internat J Numer Methods Engrg 2023;124:1798–817.
[39] Dadgar-Rad F, Hossain M. Large viscoelastic deformation of hard-magnetic soft beams. Extrem Mech Lett 2022b;54:101773.
[40] Liu J, Yang Y, Li M, Xu F. A meshfree model of hard-magnetic soft materials. Int J Mech Sci 2023;258:108566.
[41] Yang Y, Li M, Xu F. A solid-shell model of hard-magnetic soft materials. Int J Mech Sci 2024;271:109129.
[42] Zhang R, Wu S, Ze Q, Zhao R. Micromechanics study on actuation efficiency of hard-magnetic soft active materials. J Appl Mech 2020;87:091008.
[43] Mukherjee D, Rambausek M, Danas K. An explicit dissipative model for isotropic hard magnetorheological elastomers. J Mech Phys Solids 2021;151:104361.
[44] Ye H, Li Y, Zhang T. Magttice: A lattice model for hard-magnetic soft materials. Soft Matter 2021;17:3560–8.
[45] Wang L, Kim Y, Guo CF, Zhao X. Hard-magnetic elastica. J Mech Phys Solids 2020;142:104045.
[46] Li M, Yang Y, Cheng Z, Xu F. A model of hard-magnetic soft curved beams at large deformation. Chin Sci Bull 2022;67:4080–91.
[47] Yan D, Abbasi A, Reis PM. A comprehensive framework for hard-magnetic beams: Reduced-order theory, 3D simulations, and experiments. Int J Solids Struct 2022;257:111319.
[48] Sano TG, Pezzulla M, Reis PM. A Kirchhoff-like theory for hard magnetic rods under geometrically nonlinear deformation in three dimensions. J Mech Phys Solids 2022;160:104739.
[49] Yang Y, Li M, Xu F. A 3D hard-magnetic rod model based on co-rotational formulations. Acta Mech Sin 2022;38:222085.
[50] Yang Y, Xu F. Computational morphology and morphogenesis for empowering soft-matter engineering. Nat Comput Sci 2024;4:388–90.
[51] Yue L, Sun X, Yu L, Li M, Montgomery SM, Song Y, et al. Cold-programmed shape-morphing structures based on grayscale digital light processing 4D printing. Nat Commun 2023;14:5519.
[52] Ying X, Fernando D, Dias MA. Inverse design of programmable shape-morphing kirigami structures. Int J Mech Sci 2025;286:109840.
[53] Hanuhov T, Cohen N. Design principles for 3D-printed thermally activated shape-morphing structures. Int J Mech Sci 2024;262:108716.
[54] Chen T, Yang X, Wang Y. Design and modeling of a programmable morphing structure with variable stiffness capability. Int J Mech Sci 2024;284:109699.
[55] Sun Y, Song K, Ju J, Zhou X. Curved-creased origami mechanical metamaterials with programmable stabilities and stiffnesses. Int J Mech Sci 2024;262:108729.
[56] Wan H, Chang J, Ye F, Fan Z. Shape programming of porous bilayer hydrogel structures. J Appl Mech 2024;91:081010.
[57] Li W, Zhang XS. Arbitrary curvature programming of thermo-active liquid crystal elastomer via topology optimization. Comput Methods Appl Mech Engrg 2023;417:116393.
[58] Wang C, Zhao Z, Zhang XS. Inverse design of magneto-active metasurfaces and robots: Theory, computation, and experimental validation. Comput Methods Appl Mech Engrg 2023;413:116065.
[59] Zhao Z, Zhang XS. Topology optimization of hard-magnetic soft materials. J Mech Phys Solids 2022;158:104628.
[60] Zhao Z, Zhang XS. Encoding reprogrammable properties into magneto-mechanical materials via topology optimization. Npj Comput Mater 2023;9:57.
[61] Zhao Z, Wang C, Zhang XS. Multiphysics topology optimization of magnetic materials with continuous magnetization orientations. Mech Mater 2024;198:105089.
[62] Chen W, Yan Z, Wang L. On mechanics of functionally graded hard-magnetic soft beams. Internat J Engrg Sci 2020;157:103391.
[63] Audoly B, Pomeau Y. Elasticity and geometry. Oxford: Oxford University Press; 2010.
[64] Lang H, Arnold M. Numerical aspects in the dynamic simulation of geometrically exact rods. Appl Numer Math 2012;62:1411–27.
[65] Yan D, Aymon BFG, Reis PM. A reduced-order, rotation-based model for thin hard-magnetic plates. J Mech Phys Solids 2023;170:105095.
[66] Zhang Y, Ma Y, Yu J, Gao H. Non-contact actuated snap-through buckling of a pre-buckled bistable hard-magnetic elastica. Int J Solids Struct 2023;281:112413.
[67] Stewart EM, Anand L. Magneto-viscoelasticity of hard-magnetic soft-elastomers: Application to modeling the dynamic snap-through behavior of a bistable arch. J Mech Phys Solids 2023;179:105366.
[68] Dorfmann L, Ogden RW. Hard-magnetic soft magnetoelastic materials: Energy considerations. Int J Solids Struct 2024;294:112789.
[69] Danas K, Reis PM. Stretch-independent magnetization in incompressible isotropic hard magnetorheological elastomers. J Mech Phys Solids 2024;191:105764.
[70] Moreno-Mateos MA, Danas K, Garcia-Gonzalez D. Influence of magnetic boundary conditions on the quantitative modelling of magnetorheological elastomers. Mech Mater 2023;184:104742.
[71] Argyris J. An excursion into large rotations. Comput Methods Appl Mech Engrg 1982;32:85–155.
[72] de Borst R, Crisfield MA, Remmers JJC, Verhoosel CV. Nonlinear finite element analysis of solids and structures. New York: Wiley; 2012.
[73] Bai Y, Wang H, Xue Y, Pan Y, Kim JT, Ni X, et al. A dynamically reprogrammable surface with self-evolving shape morphing. Nature 2022;609:701–8.
[74] Cheng X, Fan Z, Yao S, Jin T, Lv Z, Lan Y, et al. Programming 3D curved mesosurfaces using microlattice designs. Science 2023;379:1225–32.
[75] Ma J, Zhang TY, Sun S. Machine learning-assisted shape morphing design for soft smart beam. Int J Mech Sci 2024;267:108957.
[76] Shen Z, Hu X, Tang Z, Xiao Y, Wang S, Cheng X, et al. Curvature programming of freestanding 3D mesostructures and flexible electronics based on bilayer ribbon networks. J Mech Phys Solids 2024;191:105766.
[77] Peng XL, Xu BX. Data-driven inverse design of composite triangular lattice structures. Int J Mech Sci 2024;265:108900.
[78] Perez-Garcia C, Zaera R, Aranda-Ruiz J, Bordiga G, Risso G, Lopez-Donaire ML, et al. Reprogrammable mechanical metamaterials via passive and active magnetic interactions. Adv Mater 2025;2412353.
[79] Ren Z, Hu W, Dong X, Sitti M. Multi-functional soft-bodied jellyfish-like swimming. Nat Commun 2019;10:2703.
[80] Ko Y, Na S, Lee Y, Cha K, Ko SY, Park J, Park S. A jellyfish-like swimming mini-robot actuated by an electromagnetic actuation system. Smart Mater Struct 2012;21:057001.
[81] Nandan S, Sharma D, Sharma AK. Viscoelastic effects on the nonlinear oscillations of hard-magnetic soft actuators. J Appl Mech 2023;90:061001.
[82] Lamini C, Benhlima S, Elbekri A. Genetic algorithm based approach for autonomous mobile robot path planning. Procedia Comput Sci 2018;127:180–9.
[83] Bajpai P, Kumar M. Genetic algorithm–an approach to solve global optimization problems. Indian. J Comput Sci Eng 2010;1:199–206.

[84] Liu X, Jiang D, Tao B, Jiang G, Sun Y, Kong J, et al. Genetic algorithm–based trajectory optimization for digital twin robots. Front Bioeng Biotech 2022;9:793782.
[85] Zhang J-R, Zhang J, Lok T-M, Lyu MR. A hybrid particle swarm optimization-back-propagation algorithm for feedforward neural network training. Appl Math Comput 2007;185:1026–37.
[86] Pang H, Liu F, Xu Z. Variable universe fuzzy control for vehicle semi-active suspension system with MR damper combining fuzzy neural network and particle swarm optimization. Neurocomputing 2018;306:130–40.
[87] Jiao J, Ghoreishi S, Moradi Z, Oslub K. Coupled particle swarm optimization method with genetic algorithm for the static-dynamic performance of the magneto-electro-elastic nanosystem. Eng Comput- Ger 2022;38:2499–513.
[88] Samma H, Mohamad-Saleh J, Suandi SA, Lahasan B. Q-learning-based simulated annealing algorithm for constrained engineering design problems. Neural Comput Appl 2020;32:5147–61.
[89] Haznedar B, Kalinli A. Training ANFIS structure using simulated annealing algorithm for dynamic systems identification. Neurocomputing 2018;302:66–74.
[90] Hosseini FS, Choubin B, Mosavi A, Nabipour N, Shamshirband S, Darabi H, et al. Flash-flood hazard assessment using ensembles and Bayesian-based machine learning models: Application of the simulated annealing feature selection method. Sci Total Environ 2020;711:135161.